

1 **Anatomy of a fumarole field; drone remote sensing and petrological**
2 **approaches reveal the degassing and alteration structure at La Fossa**
3 **cone, Vulcano Island, Italy**

4 Daniel Müller¹, Thomas R. Walter¹, Valentin R. Troll^{2,3}, Jessica Stammeier¹, Andreas Karlsson⁴, Erica
5 de Paolo⁵, Antonino Fabio Pisciotta⁶, Martin Zimmer¹, Benjamin De Jarnatt¹

6
7 ¹GFZ German Research Centre for Geosciences, Telegrafenberg, 14473 Potsdam, Germany

8 ²Dept. of Earth Sciences, Natural Resources and Sustainable Development, Uppsala University, Sweden

9 ³Istituto Nazionale di Geofisica e Vulcanologia (INGV), Rome, Italy

10 ⁴Department of Geosciences, Swedish Museum of Natural History, Box 50007, SE-104 05 Stockholm, Sweden

11 ⁵University of Milano-Bicocca, Department of Earth and Environmental Sciences, Piazza della Scienza 4 – 20126 Milano,
12 Italy

13 ⁶Istituto Nazionale di Geofisica e Vulcanologia (INGV), Palermo, Italy

14 *Correspondence to:* Daniel Müller (dmueller@gfz-potsdam.de)

15

16

17

18

19

20

21

22

23

24

25

26

27

28

29

30

31 **Abstract.** Hydrothermal alteration and mineralization processes can affect the physical and chemical properties of volcanic
32 rocks. Aggressive acidic degassing and fluid flow often also leads to changes in the appearance of a rock, such as changes in
33 surface coloration or intense bleaching. Although hydrothermal alteration can have far-reaching consequences for rock stability
34 and permeability, yet limited knowledge exists on the detailed structures, extent, and dynamic changes that take place near the
35 surface of hydrothermal venting systems. By integrating drone-based photogrammetry with mineralogical and chemical
36 analyses of rock samples and surface gas flux, we investigate the structure of the evolving volcanic degassing and alteration
37 system at the La Fossa cone on the island of Vulcano, Italy. Our image analysis combines Principal Component Analysis
38 (PCA) with image classification and thermal analysis, through which we identify an area of approximately 70,000 m² that
39 outlines the maximum extent of hydrothermal alteration effects at the surface, represented by a shift in rock color from reddish
40 to gray. Within this area, we identify distinct gradients of surface coloration and temperature that indicate a local variability
41 of degassing and alteration intensity and define several structural units within the fumarole field. At least seven of such larger
42 units of increased activity could be constrained. Through mineralogical and geochemical analysis of samples from the different
43 alteration units, we define a relationship between surface appearance in drone imagery and the mineralogical and chemical
44 composition. Gradients in surface color from reddish to gray correlate with a reduction of Fe₂O₃ from up to 3.2% in the
45 unaltered regime to 0.3% in the altered regime, and the latter coincides with the area of increased diffuse acid gas flux. As the
46 pixel brightness increases towards higher alteration gradients, we note a loss of the initial (igneous) mineral fraction and a
47 change in bulk chemical composition with a concomitant increase in sulfur content from close to 0% in the unaltered samples
48 to up to 60% in samples from the altered domains. Using this approach of combined remote sensing and in situ analyses, we
49 define and spatially constrain several alteration units and compare them to the present-day thermally active surface and
50 degassing pattern over the main crater area. The combined results permit us to present a detailed anatomy of the La Fossa
51 fumarole field, including high-temperature fumaroles and seven larger units of increased alteration intensity, surface
52 temperature, and variably intense surface degassing. Importantly, we also identify apparently sealed surface domains that
53 prevent degassing, likely as a consequence of mineral precipitation from degassing and alteration processes. By assessing the
54 thermal energy release of the identified spatial units quantitatively, we show that thermal radiation of high-temperature
55 fumaroles accounts for < 50% of the total thermal energy release only, and that the larger part is emitted by diffuse degassing
56 units. The integrated use of methods presented here has proven to be a useful combination for a detailed characterisation of
57 alteration and activity patterns of volcanic degassing sites and has potential for application in alteration research and for
58 monitoring of volcanic degassing systems.

59

60 **1 Introduction**

61 **1.1 Volcanic degassing and hydrothermal alteration**

62 Volcanic degassing at the Earth's surface is typically expressed in the form of localized fumarole fields and diffuse degassing.
63 Yet, the association of localized and diffuse degassing is not well constrained. A fumarole is a vent or opening in the Earth's
64 surface that releases steam and gas, including sulfur dioxide, carbon dioxide, and hydrogen sulfide, into the atmosphere (e.g.
65 Giggenbach, 1996; Giammanco et al., 1998; Halldorsson et al., 2013). Fumaroles are typically found near volcanic areas or
66 geothermal regions where there is intense heat beneath the surface. Fumaroles are of interest to scientists studying volcanoes
67 and geothermal systems, as they provide information on the composition of underlying magmatic systems, the degassing
68 processes of such magmatic systems, and the dynamic changes in the degassing pathways exploited by such systems (e.g.
69 Chiodini et al., 1993; Aiuppa et al., 2005; Paonita et al., 2013). The gas emissions by fumaroles, moreover, provide information
70 on the possible interaction between underground water and hot rocks or magma and thus the state of a hydrothermal system
71 through time (e.g. Chiodini et al., 1993; Capasso et al., 2000; Nuccio et al., 2001; Troll et al., 2012; Paonita et al., 2013).

72 The degassing of hot and acid volcanic gasses leads to versatile fluid-rock interactions at the surrounding volcanic rock,
73 summarized as hydrothermal alteration (Pirajno, 2009; Chiodini et al., 2013; Fulignati, 2020). Alteration can affect the mineral
74 assemblage by dissolution and remineralization up to complete destruction of the original mineral matrix and eventually
75 influence essential rock parameters with potentially far-reaching consequences for the shallow hydrothermal system and the
76 stability of a volcanic building (Reid and Brien, 2001; Heap and Violay, 2021). Mechanical strength tests of hydrothermally
77 altered rocks showed considerable mechanical weakening (e.g. Frolova et al., 2014; Heap et al., 2021a, Darmawan et al., 2022),
78 which is usually accomplished by mineral dissolution and mineral re-precipitation that affect rock strength and permeability
79 and can in cases even seal gas pathways. Hydrothermal alteration can thus lead to sealed rock masses and hence to pressure
80 build-up in a shallow volcanic system and consequently influence volcanic activity (e.g. Heap et al., 2019) and increase the
81 likelihood of flank deformation and collapse (Heap et al., 2021b). It is therefore important to better understand the degassing
82 and alteration structures in active hydrothermal crater regions of hazardous volcanic systems.

83 In this study of the fumaroles of La Fossa cone, Vulcano Island - Italy, we aim to detect and quantify alteration-related spatial
84 and compositional parameters in order to provide improved insight into the dynamic changes of hydrothermal venting systems
85 to help identify temporal and potentially critical developments and to better understand the associated features of diffuse and
86 localized degassing.

87

88 **1.2 Structure and extent of degassing sites**

89 Recent advances in volcanic geothermal areas suggest that fumaroles are often only localized expressions of a much larger
90 area of degassing (e.g. Toutain et al., 2009; Liuzzo et al., 2015). Indeed, fumaroles and hydrothermal degassing zones are often
91 accompanied by broader fields of activity, characterized by diffuse degassing processes, associated mineral changes, and

92 intense surface recoloration (e.g. Donoghue et al., 2008; Berg et al., 2018; Darmawan et al., 2022) and fumaroles activity can
93 vary in time (Troll et al., 2012; Fischer et al., 2015) and in size (Lynch et al., 2013; Gertisser et al 2023). Previous works at
94 Vulcano, for instance, have shown that fumaroles are surrounded by extensive areas of diffuse degassing (Carapezza et al.,
95 2011; Chiodini et al., 2005; Manini et al., 2019). Our previous work showed that diffuse degassing leads to distinct zones of
96 activity that can be identified by temperatures and visual expression (Müller et al., 2021). Those diffuse zones are typically
97 constrained based on CO₂ measurements but are also subject to the diffuse flow of acid gas driving diffuse alteration processes.
98 However, these diffuse degassing and alteration processes are often difficult to recognize without specialized sampling
99 strategies (Toutain et al., 2009), leading to a limited understanding of the anatomy and extent of degassing and alteration
100 systems. Understanding the dynamic changes and internal architecture of hydrothermal activity of fumarole fields and the true
101 dimensions of their field of activity is of relevance for the study of volcanic activity and hazard potential.
102

103 **1.3 Surface effects and remote sensing of alteration**

104 Hydrothermal alteration can cause significant changes in the physical and chemical properties of volcanic rock, such as density,
105 compressive strength, and permeability (e.g. Donoghue et al., 2008, 2010; Berg et al., 2018; Heap et al., 2019; Darmawan et
106 al., 2022). The replacement of primary minerals by secondary minerals, element mobility of fluid-mobile components,
107 enrichment of refractory elements, and physical and textural changes of rock properties are often accompanied by changes in
108 the color or spectral reflectance characteristics and can be traced employing remote sensing techniques.

109 Several studies have investigated the relationship between coloration and hydrothermal alteration. The use of rock color or
110 spectral reflectance particularities as an indicator of alteration has been explored since the 1970s and led to the development
111 of a variety of satellite remote sensing techniques using ETRS multispectral imagery (Rowan et. al., 1976), Landsat Thematic
112 Mapper mission (Carranza et al., 2002), ETM+ (Mia et al., 2012), ASTER data (Di Tommaso et al., 2007) or hyperspectral
113 data (e.g. Van De Meer et al., 2012; Tayebi et al., 2015). These techniques can detect subtle changes in color that may not be
114 visible to the naked eye, allowing for the identification of mineral deposits (Mielke et al., 2016), hydrothermal alteration, or
115 volcano stability (Kereszturi et al., 2020).

116 However, for analyzing details of localized degassing and alteration systems, the resolution of satellite data is often a limiting
117 factor. Some of the best available optical satellite data have a resolution of 0.5 m in the nadir acquisition position. The
118 resolution of thermal satellite data is on the order of tens to hundreds of meters per pixel. That allows the general detection of
119 degassing and alteration systems, but the imaging of details of such systems requires the use of very high-resolution data.
120 Modern UAS (unmanned aerial systems) equipped with high-resolution sensors allow imaging of volcanic surfaces at cm
121 scales and, therefore, permit the analysis of degassing and alteration systems in great detail. In combination with Structure
122 from Motion (SfM) processing, they are efficient for first-site investigations and allow the creation of high-resolution structural
123 maps to identify structures of degassing systems to assist first-order hazard analysis or guide further in-depth studies.

124 **1.4 Aim of the study**

125 The aim of this work is to image and analyze the degassing and alteration structure of the La Fossa fumarole field and the
126 wider field of activity and better understand the association of diffuse and localized degassing and alteration at degassing sites.
127 We advance previous results (Müller et al., 2021) by considering new data, and by integrating them with the mineralogical
128 and chemical analysis of alteration distribution in collected rock samples. We show systematic changes in the effects of
129 alteration on the surface coloration and how drone-derived RGB data (Red, Green, Blue, standard color coding of images) can
130 be used for the efficient detection and classification of degassing and alteration features. Combining UAS-based optical and
131 infrared remote sensing with mineralogical- and geochemical analysis, and diffuse surface degassing measurements, we can
132 infer the detailed anatomy of degassing and alteration systems at the surface, highlight active degassing domains versus areas
133 of surface sealing, and determine their importance for the system based on their contribution to the total thermal energy release.

134 **2 Study area**

135 Vulcano is the southernmost of a group of 7 volcanic islands forming the Aeolian Archipelago north of Sicily. They are located
136 within the Aeolian Tindari Letojanni Fault System (ATLFS), an NNW-SSE striking local deformation belt connecting the
137 central Aeolian Islands with the eastern section of Sicily (Barreca et al., 2014; Cultrera et al., 2017). The ATLFS is the interface
138 between two larger tectonically active compartments, an extensive one in the northeast and a contractional one in the west
139 (Cultrea et al., 2017). Frequent seismic activity and right lateral extensional displacements indicate ongoing tectonic activity
140 (Billi et al., 2006) and the active shaping of the islands.

141 Vulcano is made up of volcanic edifices of which the northern section of the islands is the most recently active. The oldest
142 volcanic activity at Vulcano is reported for 130 ka (De Astis et al., 2013). Six main stages of volcanic activity have been
143 identified (De Astis et al. 1997), of which the geologically younger active parts, the La Fossa Cone and Vulcanello, have been
144 active during historical times < 8 ka, showing mainly vulcanian and strombolian activity (De Astis et al., 2013). The last
145 eruptive period of the La Fossa Cone from 1888-1890 was characterized by strong phreatic eruptions and witnessed and
146 documented by Giuseppe Mercalli who later coined the term Vulcanian eruptions (Clarke et al., 2015).

147 Vulcano since then has been in a quiescent period and volcanic activity mainly expressed in degassing. Gasses are provided
148 from a magmatic-hydrothermal system fed by a shallow magmatic reservoir beneath La Fossa volcano. The hydrothermal
149 system is likely to have been partitioned into a hypersaline brine and a vapor phase (Henley and McNabb, 1978). The denser
150 brine phase is confined at depth and contributes to the formation of metasomatic facies observed in deep-seated xenoliths
151 (Adrian et al., 2007). The vapor phase, enriched with SO₂, H₂S, HCl, and HF, ascends to the surface and partly emerges directly
152 from the high-temperature fumarolic field (Bolognesi and D'Amore, 1993; Chiodini et al., 2000; Capasso et al., 1997).

153 Volcanic degassing is present throughout the entire central and northern part of the island concentrating in degassing clusters
154 at Baja Di Levante, within Vulcano Porto, and in clusters along the base and summit of La Fossa Cone (Chiodini et al., 1996;

155 Carapezza et al., 2011; Diliberto et al., 2021; Inguaggiato et al., 2022 and many others) where frequently higher fluxes of CO₂
156 are observed. The most prominent degassing sites are the high-temperature fumaroles at the summit of Vulcano that occur in
157 several clusters on the outer rims of La Fossa cone and are most prominent in the high-temperature fumarole field (Figure 1).
158 Degassing at the summit of La Fossa is persistent but subject to fluctuations. Gasses of the high-temperature fumaroles (HTF)
159 emerge with temperatures > 300 °C, but temperatures have been exceeded during previous volcanic crises (Harris et al., 2012;
160 Diliberto, 2017). Temperatures of up to 690 °C were reported in May 1993 by Chiodini et al. (1995).
161 Periods of unrest were accompanied by increasing fumarole temperatures (Harris et al., 2012; Diliberto, 2013; Madonia et al.,
162 2013; Diliberto, 2017), increasing soil and groundwater temperatures (Capasso et al., 2014), changing gas compositions
163 (Paonita et al., 2013), changes in gas flux (Inguaggiato et al., 2022), or a spatial growth of the fumarole field (Bukomirovic et
164 al., 1997). The most recent crisis occurred in 2021 and led to increased thermal radiation (Coppola et al., 2022), deformation
165 (INGV Bulletin reports), and localized structural changes like the formation of new major fumarole complexes. The rapid
166 dynamics during volcanic crises and potentially negative effects of alteration on permeabilities, and therewith the potential to
167 drain gasses from the surface, highlight the importance of a better understanding of the structure and state of degassing systems.
168 Early studies about the structural setup of the Grand Cratere fumarole field of the La Fossa Cone were provided by
169 Bukomirovic et al. (1997) and later modified (Madonia et al., 2016; Harris et al., 2009). Fulignati et al. (1999) analyzed
170 alteration facies at Vulcano and constrained the central crater region to be a large silicic alteration complex characterized by
171 the presence of chalcedony and amorphous silica. Outwardly to the central silicic alteration zone, advanced argillic (alunite ±
172 gypsum) alteration develops, probably originating from the progressive neutralization of the acid fluids by weathering and
173 dilution by meteoric waters (Fulignati et al., 1998). Müller et al. (2021) previously showed that degassing and alteration can
174 be traced from remote sensing data far beyond the extent of the high-temperature fumarole locations. Based on surface color
175 variability due to degassing and alteration processes, they showed evidence for a more complex setup with alteration gradients
176 within the silicic alteration complex and important structural units that will be complemented here. Examples of degassing and
177 alteration-related surface color variability are shown in Figure 2.

178 **3 Data and methods**

179 To analyze the degassing and alteration structure at Vulcano, we used a combination of UAS-derived remote sensing data
180 (optical and thermal infrared imagery), image analysis, and field-based ground-truthing by mineralogical and geochemical
181 analysis of rock samples and surface degassing measurements. A simplified sketch of the workflow is shown in Figure 3.

182 1) An anomaly detection (Chapter 3.2) based on UAS-derived data, employing image analysis techniques like Principal
183 Component Analysis (PCA), and spectral and thermal classification (similar to Müller et al., 2021) provides the detailed optical
184 and thermal anomaly pattern. Anomalies can be revealed based on slight color changes in the volcanic surface that occur due
185 to degassing and hydrothermal alteration processes, or increased surface temperatures.

186 2) To verify observed anomalies, we carried out ground-truthing by mineralogical (XRD - X-ray diffraction) and geochemical
187 (XRF - X-ray fluorescence) lab analyses of representative rock samples. Further, we performed surface degassing
188 measurements to image the present-day degassing pattern and compared it to the observed anomaly pattern. Combining this
189 information we can infer a detailed anatomy of the degassing and alteration structure at the surface and define and parameterize
190 major structural units.

191 3) A temporal infrared monitoring carried out from 2018 to 2022, covering the volcanic crisis 2021 at Vulcano, allows us to
192 monitor the thermal evolution and response of the identified units to an event of increased gas flow with further implications
193 of critical processes like localized surface sealing. Details on the single analysis steps are provided below.

194 The remote sensing data used for this study and relevant processing steps are published in a Zenodo data repository
195 <https://doi.org/10.5281/zenodo.12586672>.

196

197 **3.1. Acquisition and processing of UAS-based optical and thermal infrared data**

198 The data acquisition was performed using a DJI Phantom 4 Pro quadcopter, equipped with a gimbal-stabilized 20 MP camera
199 with a real shutter system, recording up to 0.5 HZ. Optical overflights were performed in the daytime at an altitude of 150 m
200 above the fumarole field, ensuring a minimum overlap of 90% for later photogrammetric processing. Thermal infrared image
201 data was acquired by a Flir Tau 2 radiometric thermal infrared camera system attached to the DJI Phantom 4 Pro. The FLIR
202 Tau 2 measures in the spectral range of thermal infrared between 7.5 and 13 μm , has a resolution of 640 x 512 pixels, and is a
203 fully radiometric sensor system. The infrared image data is recorded at 8 Hz by a Teax Thermal Capture 2 data logger. The
204 camera was attached to the copter with a standard camera bracket on a self-made carrier frame and is powered by an external
205 11.1 V lithium-polymer battery, supplying voltage to the camera system (transformed down to 5.2 V in) and to an external
206 GPS antenna (> 8 V required) which provides coordinates for each infrared image. Infrared overflights were performed in the
207 early morning hours, before the sun illuminates the crater area, to avoid disturbances of irregular surface heating due to solar
208 radiation exposure (Stevenson and Varley, 2008). In this way, we ensure to map the thermal signal from the hydrothermal
209 system exclusively.

210 All image data were processed using the Structure from Motion (SfM) approach in Agisoft Photoscan (Version 1.5.2.7838).
211 The image data were inspected and images were preselected ensuring an overlap of 90%. Images of poor quality or out of
212 focus were excluded and only images of a constant flight altitude were used for the processing. This is particularly important
213 for the processing of infrared data, as varying altitudes might alter the radiation information due to changing pixel size to vent
214 ratios. The infrared data was pre-inspected in Thermoviewer 3.0 and exported in a 16-bit tiff format in grayscale. We followed
215 the typical workflow of sparse point cloud-, dense point cloud- and mesh generation, aiming to obtain a 3-dimensional model
216 and eventually orthomosaic, digital elevation model (DEM), and infrared mosaic. The original images and processing results
217 are roughly georeferenced, but their geolocation was optimized by manual co-registration using the ArcGIS georeferencing
218 toolbox. An overview of the acquired and processed data sets can be found in Table 1.

220 **3.2 Anomaly detection - Principal Component Analysis (PCA) and spectral classification for alteration mapping**

221 The alteration mapping was performed on an orthomosaic data set acquired in 2019 that due to poor fumarole activity provides
222 an almost distortion-free image of the central crater region. The alteration structure was revealed, similar to Müller et al.
223 (2021), by applying a Principal Component Analysis and image classification allowing further constraints on the zonation of
224 the fumarole area and expanding the interpretation by geochemical and mineralogical analyses of rock samples for ground
225 truthing. PCA is a statistical tool that was invented by Pearson (1901), further developed and widely applied in remote sensing
226 or image analysis (e.g. Loughlin, 1991; Fauvel et al., 2009; Alexandris et al., 2017). It can detect and highlight optical
227 anomalies within an RGB data set by transforming the data values of the initial RGB channels onto their perpendicular axes
228 of the highest data variance (e.g. Abdi and Williams, 2010). This can be achieved in several ways. We used the PCA
229 implemented in the ArcGIS image analysis toolbox (see ArcGIS online documentation for Principal Component Analysis),
230 performing the following workflow. In the first step, an ellipse including all data points is calculated for each dimension
231 (RGB). The main axes of these ellipses represent the Eigenvectors (direction of highest variance), and will be used as a new
232 coordinate system for the data transformation. By transforming all data points onto this new coordinate system, we obtain
233 Principal Components (PC) which are variance representations of the initial RGB bands and can be used to detect and highlight
234 optical anomalies like color changes due to alteration processes (Müller et al., 2021, Darmawan et al., 2022). PCA further
235 promotes a decorrelation of the initial RGB bands, a dimensionality reduction, and associated better data separability so that
236 color variations, before expressed by changes in the three RGB bands (3-dimensional problem), can now be accessed in single
237 bands, the single Principal Components (PC). While Principal Component 1 (PC) resembles 91% of the initial data variance,
238 it mainly shows brightness changes within the image. PC 2 and 3 contain 7% and 2% of the data variance, resemble color
239 changes, and are suitable to resolve optical anomalies related to hydrothermal alteration.

240 In our data, hydrothermally altered areas were defined based on the PC3, with pixel values > 85 representing hydrothermal
241 alteration. We used this as a mask to crop the respective pixel locations from the original orthomosaic (RGB), resulting in a
242 16 Mio pixel alteration raster subset (RGB). This alteration raster subset allows for a more sensitive image analysis due to the
243 reduced spectral range with respect to the original orthomosaic. Another iteration of PCA, now applied to the extracted
244 alteration raster subset adjusts to the new reduced spectral range, as we are excluding all redundant data e.g. unaltered surface,
245 and provide a variance representation of the altered surface exclusively. We classified the result in an unsupervised
246 classification (implemented in ArcGIS, using a combination of Iso Cluster and Maximum Likelihood classification) with 32
247 classes. We decided on unsupervised classification as this is a more data-explorative way of exploring the pixel information,
248 rather than classifying based on a spectral range constrained by training areas defined on pre-assumptions in a supervised
249 classification. The 32 classes are chosen to obtain a high class resolution, as this is the highest number of classes possible in
250 the unsupervised classification tool. By combining these classes in a way that they resemble larger optical spatial units, we

251 eventually defined 3 Types of alteration surface (Types 1 - 3) and the unaltered surface (Type 4) and further analyzed their
252 spectral characteristics and spatial distribution. Boxplots of the distribution of RGB values in the 32 classes and the spectral
253 range of Type 1 - 4 surfaces are shown in Appendix A. The optical structure of the fumarole field and alteration zone is similar
254 to the thermal structure and will be discussed in Chapter 4.2.

255

256 **3.3 Infrared analysis - thermal structure and time series analysis**

257 The SfM-derived infrared mosaic represents the thermal radiation in a 16-bit tiff format, resembling values between 0 and
258 65536. To obtain a temperature map from the IR mosaic we calculated the apparent pixel temperatures T_p by

$$259 \quad T_p \text{ (in K)} = \text{grayvalue} * 0.04 \quad (1)$$

260

261 where T_p is the apparent pixel Temperature in K, the gray value is the radiation value of the original infrared mosaic and 0.04
262 is the scaling factor (radiometric resolution). The temperature map was used to define the thermal structure. We observed
263 several distinct thermal spatial units with temperatures significantly above the background temperature, that can be
264 distinguished in high-temperature fumaroles (HTF in the following) and areas of rather diffuse thermal surface heating (Figure
265 4 B/D). To constrain these units spatially for further comparison, we had to approximate spatial boundaries what was done
266 after comparison to our optical data and based on knowledge of previous observations by defining the temperature thresholds
267 of $T = 22 - 40 \text{ }^\circ\text{C}$ for the diffuse heated areas and $T > 40 \text{ }^\circ\text{C}$ for HTF. The $40 \text{ }^\circ\text{C}$ threshold resembles well the known locations
268 and extent of HTF in the upper and lower fumarole field. To compare the thermal emissions of detected structural units, we
269 calculate the radiant exitance values by applying the modified Boltzmann law.

$$270 \quad Q = e * b * A * (T_p^4 - T_o^4) \quad (2)$$

271 The emissivity (e) was assumed to be 0.95 (often used as an assumption for volcanic surfaces), the Boltzmann constant (b) is
272 $5.670737 \times 10^{-8} \text{ Wm}^{-2}\text{K}^4$, the area of a pixel (A) is 0.024 m^2 . T_p is the pixel temperature and T_o is the average background
273 mean temperature, calculated based on 9 reference areas that are anomaly-free. To compare identified units quantitatively, we
274 summarized the radiation per pixel for the respective units a - g to a cumulative thermal radiation (R_{cum}). The flight altitude
275 of 150 m (above the fumarole field) in combination with the low resolution of infrared sensors results in a pixel resolution of
276 $0.38 \times 0.38 \text{ m}$.

277 Note that remotely sensed Infrared data always represents apparent temperatures that might differ from the real object
278 temperature due to the radiation properties of the measured object itself (emissivity), the distance of the sensor to the measured
279 object, the pixel-to-object size ratio, but also due to atmospheric or hydro-meteorological effects (Ball and Pinkerton, 2006)
280 influencing the detected radiation values. Therefore apparent temperatures typically are lower than in situ vent temperatures.

281 Real fumarole vent temperatures can reach more than 300 °C (Diliberto, 2013) while temperatures in our infrared mosaic range
282 to max. 163 °C only. With this data set, we do not aim to provide precise fumarole temperatures but to analyze the thermal
283 structure of the fumarole field and the broader field of activity.

284

285 **3.4 Ground-truthing by Mineralogical and Geochemical Analysis**

286 **3.4.1 Rock sampling**

287 Rock samples were collected at predefined representative locations aiming to include all alteration end members, during field
288 campaigns in 2019 and 2022. We sampled along 3 transects following the postulated hydrothermal alteration gradients and
289 crosscutting major alteration units, of which transect A is located on the lower fumarole field, transect B along the upper crater
290 rim, and transect C in the eastern fumarole field (locations for samples in Figure 7). Samples were in the size of ~2000 cm³
291 (hand-sized) retaining the undisturbed surface crust, but also subsurface material to a depth of ~10 cm. The samples were
292 mechanically crushed, ground to 63 µm, and split for XRD and XRF analysis, respectively. In total 21 samples were collected
293 of which 9 were prepared for the XRD and XRF analysis and 12 for XRF analysis exclusively.

294 **3.4.2 X-ray diffraction (XRD)**

295 Between 1 and 3 mg of whole rock powder was used to determine the mineral composition of each sample through powder X-
296 ray diffraction (pXRD). The analysis was conducted using a PANalytical X'pert diffractometer equipped with an X'Celerator
297 silicon-strip detector at the Department of Geoscience, Swedish Museum of Natural History, Stockholm. The instrument was
298 operated at 45 kV and 40 mA using Cu-K α radiation ($\lambda = 1.5406 \text{ \AA}$). Samples were analyzed between 5° and 70° (2 θ) for 20
299 min in step sizes of 0.017° in continuous scanning mode while rotating the sample. Data were collected with "divergent slit
300 mode" and converted to "fixed slit mode" for Rietveld refinement. The collected data show several peaks of X-ray diffraction
301 intensity which represent the characteristic of crystalline minerals, the proportions of mineral phases were then refined using
302 the Rietveld refinement method in the High Score Plus 4.6e software. The XRD analytical procedure was performed twice for
303 each sample to ensure optimal quality control. Some samples contained contents of amorphous material of more than 50%.
304 Those will be marked with a * in the following but we will consider the mineral composition normalized to 100% non-
305 amorphous material.

306 **3.4.3 X-ray fluorescence (XRF)**

307 Bulk chemical composition was determined by X-ray fluorescence analysis (XRF) at the EIMiE Lab at the German Center for
308 Geosciences (GFZ). Main and trace elements were measured on fused beads with an AXIOS spectrometer (Malvern
309 Panalytical, UK). Loss of ignition (LOI) was determined by analysis of H₂O/CO₂ using an Eltra element analyzer.

310 Reproducibility was determined on three certified reference materials (CRM) and is within the analytical precision, which is
311 better than 2% for main elements and better than 10% for trace elements.

312 **3.4.4 Surface degassing measurements (CO₂, SO₂, H₂S)**

313 The surface degassing was measured at ~200 points within the northern part of the La Fossa cone (Figure 6) in September
314 2021 and November 2022 using a simplified Multigas accumulation chamber approach (Appendix B). The measurement unit,
315 a Dräger X-am 8000 handheld Multigas device, was equipped with 6 sensors measuring CO₂, CH₄, SO₂, H₂S, H₂, and O₂
316 simultaneously of which CO₂, SO₂, and H₂S are considered here. The simplified accumulation chamber approach was an
317 adaption as a consequence of uncertainties encountered in previous Multigas measurement campaigns. Due to different sensor
318 reaction times for ascending and especially descending gas concentrations, the comparison of direct sensor readings might
319 lead to odd gas ratios with an artificial shift towards magmatic components. For that reason, we use the slope of the ascending
320 gas concentration within a defined volume as quantification for a relative surface flow. More detailed information about the
321 gas measurement approach is provided in the supplementary materials. Note that the aim of the gas measurements was not to
322 provide accurate flux estimates but to highlight the spatial variability of the gas flow of certain gas species from the surface.

323 **4 Results**

324 **4.1 Thermal- and optical anomaly patterns reveal the degassing and hydrothermal alteration structures**

325 Degassing and hydrothermal alteration at La Fossa as seen in drone imagery can be traced by mainly two effects.

326 1) The transition from unaltered to hydrothermally altered surface can be traced by a general color shift in the drone images
327 from reddish to grayish (Figures 2A and 4A). This allowed us to constrain a distinct ~70,000 m² sized area surrounding the
328 fumarole field in a circumferential manner. This area is hereafter referred to as the Alteration Zone (ALTZ in Figure 4A/B),
329 and represents the maximum extent of at the surface observable alteration effects that can be associated with the fumarole
330 field. It includes effects ranging from weak surface alteration to strong alteration with intense surface bleaching and
331 remineralization, to complete destruction of the host material. The extent of the ALTZ exceeds the area covered by the high-
332 temperature fumarole (HTF) site by ~60 times (Figure 4A/B), indicating the widespread influence of diffuse degassing and
333 alteration processes.

334 2) Within the ALTZ we observe a segmentation characterized by brightness and color variability expressed in different shades
335 of gray (Figure 4A), the second optical effect, indicating local alteration gradients. Analyzing the ALTZ for this spectral
336 variability by PCA and image classification we can constrain pixels of low-, increased-, or intense surface bleaching and
337 alteration (light blue, dark blue, and red pixels in Figure 4B) and define an alteration index represented by 4 surface Types (1
338 - 4), of which Type 1 is the most altered and Type 4 the least altered / unaltered surface.

339 Type 1 surfaces are bright grayish intensely bleached surfaces or sulfuric deposits and represent the strongest alteration end
340 members that we can detect optically from our data. Type 1 mainly resembles the fumarole sites and surrounding areas (Figure
341 4 A/B) but also larger isolated regions that can not be associated with major vent systems. With increasing distance to the
342 degassing centers, we observe a shift towards darker grey (Type 2) and brownish (Type 3) surface colors. Type 2 is
343 characterized by a gray but comparatively less bright coloring. It typically occurs at the boundaries between Type 1 and Type
344 3 surface and largely surrounds Type 1 areas, but it also forms several isolated clusters typically embedded in Type 3 areas
345 (units b,d,g in Figure 4). Type 3 is generally darker and more reddish in color, similar to the unaltered parts of the crater
346 surface, but can be well distinguished from the unaltered surfaces by PCA. It makes up ~50% of the ALTZ and dominates in
347 the central northern and the southeastern parts. Type 4 is a reddish, apparently oxidized surface that dominates the La Fossa
348 cone surrounding the ALTZ.

349 The surfaces within the ALTZ are generally mixed and composed of more than one type. The ALTZ is characterized by a
350 generally high density of Type 3 pixels, with locally high densities of Type 1 and Type 2 pixels, which then become the
351 dominant surface Type and form larger spatial units, indicating locally higher alteration gradients or larger structural units
352 (units a - g in Figure 4 and details in Appendix C). The largest of these units cover several thousand square meters each.

353 The thermally active surface (Figure 4C) can be divided into high-temperature fumaroles (HTF in Figure 4D) and diffuse
354 thermally active surface (green pixels in Figure 4D). HTFs are the visible part of the activity that can be constrained by the
355 naked eye in the field, while the diffuse thermally active surface is largely imperceptible. The thermally active surface largely
356 mirrors the alteration pattern observed in the optical data. An analysis of the temperatures obtained at all pixels of Type 1 to 4
357 surface shows a general decrease of mean pixel temperatures from Type 1 to Type 4 surface by an average of 2 degrees (Figure
358 5). In particular, areas dominated by Type 1 and 2 surfaces reflect the thermal structure well while areas of Type 3 dominance
359 largely coincide with low-temperature surfaces (Figure 4 B/D). An additional Spearman correlation test, applied to the
360 classified surface (32 classes unsupervised, for comparison see Appendix A) and the thermal data (in °C) shows a moderate
361 positive correlation between optical and thermal anomalies (Appendix D). This shows that the detected optical anomalies are
362 meaningful and that degassing and alteration variability occurs even at local scales and can be traced in our close-range drone
363 remote sensing data.

364 The spatial coincidence of both optical and thermal anomalies highlights the relationship between variations in the surface
365 coloration, caused by alteration processes, and the ongoing influence of diffuse gas flow. A general coincidence of increasing
366 brightness (simultaneously increasing the RGB values) with increasing surface temperature of an area can be constrained
367 (Figure 5).

368 **4.2 Anomaly structure identified from optical and thermal data**

369 The optical and thermal anomalies form distinct spatial units of alteration and elevated surface temperature (units a - g in
370 Figure 4D), which now allow us to infer the following surface structure of the fumarole field and its wider field of activity.

371 The centers of degassing activity are high-temperature fumaroles (HTF). These are the “visible” parts of the activity that can
372 be perceived in the field (red pixels in Figure 4D). We spatially constrain the HTFs based on apparent temperature values with
373 $T > 40\text{ }^{\circ}\text{C}$ in our 150 m overflight data. Using this as a threshold we find that the HTFs cover an area of 1223 m², and locate
374 exclusively in the Type 1 surface. However, HTFs represent only a fraction of the active surface.

375 The total extent of the surface that has to be considered active is much larger. The surface with elevated temperature covers
376 ~30,000 m² (green pixels in Figure 4D, $T > 22\text{ }^{\circ}\text{C}$ or $5\text{ }^{\circ}\text{C}$ above the background), exceeding the area covered by HTF by a
377 factor of 25. The surface that is considered hydrothermally altered (ALTZ ~70,000 m²) exceeds the area covered by HTF by a
378 factor of ~60, highlighting the widespread influence of diffuse degassing and alteration processes.

379 Besides the HTF we have constrained larger units of elevated surface bleaching and surface temperatures that can be considered
380 structurally important and centers of diffuse degassing activity.

381 Units a and b are diffuse features of increased surface bleaching (Type 1 and 2) and surface temperature, embedded in the
382 Type 3 surface and surrounding the eastern fumarole field in the form of an aureole shape. Neither can be associated with
383 major vents. The observed maximum surface temperature for unit a is $43.7\text{ }^{\circ}\text{C}$ (0.38 m resolution) and the average temperature
384 is $25\text{ }^{\circ}\text{C}$, ~8 $^{\circ}\text{C}$ above the background. It is located at a distance of 25 to 50 m downslope from the eastern rim fumarole
385 complexes, separated by a Low-Temperature Zone (LTZ). Unit b, the southern part of the aureole is a 120 m long and 20 - 35
386 m wide anomaly located subparallel on the inner side of the crater. It extends over ~2100 m² and has a maximum surface
387 temperature of $46\text{ }^{\circ}\text{C}$ and an average temperature of $26\text{ }^{\circ}\text{C}$ (9 $^{\circ}\text{C}$ above the background). The temperature range and spatial
388 extent of units a and b are comparable. In the field, both are difficult to identify as there is little or no evidence of degassing
389 (Appendix E). Like unit a, unit b is also separated from the main fumarole vents by the LTZ. Its northern boundary corresponds
390 exactly to the positions and curvature of the fumarole alignments at a relatively constant distance of 30 meters. In unit b, we
391 observe a temperature gradient with higher temperatures at greater distances from the fumarole vents and an apparently more
392 active center in the southeastern corner. Another thermal anomaly with a similar shape and orientation is located further south
393 inside the crater.

394 Units d and f are similar aureole-like features in the western fumarole field, associated with fumarole complex F0. They
395 circumferentially surround fumarole complex F0 at a distance of 5 to 15 m, also separated from the HTF by a Low-Temperature
396 Zone (LTZ), but to a lesser extent than that observed for units a and b of the eastern fumarole field. The southwestern section
397 of this aureole, unit d, appears as a larger heated complex with stronger surface bleaching (Type 1) and higher temperature
398 (mean $T = 27\text{ }^{\circ}\text{C}$), and a temperature gradient with higher temperatures further away from the major fumarole complex. The
399 boundary to the Low-Temperature Zone is sharp with a sudden drop in temperature of 10 – 20 $^{\circ}\text{C}$ and a strong associated color
400 shift (Appendix C). The aureoles of F0 (d,f) and F11 (a,b) have in common that they are encircled by a network of polygonal
401 net-shaped thermal anomalies in the far field.

402 Low-Temperature Zones (LTZs) dominate the central parts of the fumarole field. The LTZ have only slightly elevated
403 temperatures relative to the background (18 – 21 $^{\circ}\text{C}$ or 1 – 4 $^{\circ}\text{C}$ above background) and can be optically constrained by a
404 darker Type 3 surface coloration. From field observations, we have concluded that these LTZ are strong, apparently sealed
405 surface complexes. Therefore LTZ might indicate largely sealed sections of the fumarole field which inhibit gas flow at the
406 surface. The 3 central LTZ 1 - 3 (Figure 4D) cover an area of ~12,000 m².

407 Unit c is a broad complex of highly altered material (Type 1) and significantly high surface temperatures. It is potentially the
408 most altered unit in the central crater region. It covers an area of ~8000 m² and the maximum and average apparent temperatures
409 observed are 87 °C and 29 °C. It is associated with the HTF FA and F58. Considering the thermal structure of unit c, it is a
410 heterogeneous unit composed of a network of higher temperature anomalies embedded in lower but, with respect to the
411 background, significantly increased tempered surface. This area is associated with the northwestern crater unit, which is the
412 most recent explosion crater.

413 Unit d is an area of diffuse activity associated with the inner crater part of fumarole complex F0, showing a significant shift in
414 surface colorization and temperature, some 20 m away from the fumarole complex. The boundary is distinct and visible to the
415 naked eye (Type 3 to Type 1). The temperature shift is on the order > 20 °C.

416 Unit e is a large branching thermal and optical anomaly of the upper fumarole field. It can be constrained by its gray coloration
417 embedded in the reddish unaltered surface and also by its increased surface temperature. It is a 120 – 150 m long branch-
418 shaped network of anomalies on the inner crater wall. The central feature is oriented E-W and located ~20 m south and below
419 the helicopter platform and the crater rim. We constrained its size to ~2500 m² (only the western branch, without intersection
420 to unit d) and the recorded maximum and average apparent temperatures are 45.0 °C and 25.9 °C respectively. Some smaller
421 clusters of localized degassing, alteration, and increased surface temperature, visible at the surface by its bright coloration, are
422 observed in the northern section of the fumarole field (unit g) towards La Forgia.

423 **4.3 Ground truthing - verification of observed anomalies**

425 We have carried out mineralogical (X-ray diffraction) and geochemical (X-ray fluorescence) analyses of bulk rock samples
426 collected at representative locations and surface degassing measurements. The aim is to verify the observed anomaly pattern
427 of alteration gradients and distinct active units and to investigate the relationship between the optical and thermal anomaly
428 pattern and modern degassing and hydrothermal alteration processes. In this way, we provide ground truthing and demonstrate
429 that the anomalies observed are significant.

431 **4.3.1 Present-day surface degassing pattern**

432 The measurements of diffuse degassing from the surface allow us to compare the present-day surface degassing pattern to the
433 observed optical and thermal anomalies (Figure 6 A/B). We performed surface degassing measurements of CO₂, H₂S, and SO₂
434 simultaneously in the diffuse degassing regime at 200 measurement points (~100 points within and outside the ALTZ)
435 throughout the whole northern crater section (details of gas measurements in Appendix B).

436 The observed relative flux values for CO₂ range from 0 to ~9000 ppmv/s with an average of ~900 ppmv/s. They are
437 considerably higher ($\times 10^3$) than the SO₂ and H₂S flux at the respective locations. For both, SO₂ and H₂S, a maximum gas flux
438 of < 10 ppmv/s was measured and the average is < 0.5 ppmv/s.

439 Looking at the spatial distribution of the measured gasses we observed generally higher gas levels within the alteration zone
440 ALTZ and at the ALTZ boundary, for each of the measured gasses (Figure 6 C/D). The average CO₂ flux is 660 ppmv/s outside
441 the ALTZ and 923 ppmv/s within the ALTZ. Thus, the averaged CO₂ flux inside the ALTZ is about 1.4 times higher than
442 outside but is particularly high in some of the constrained units a - g. However, the CO₂ flux has a wide spatial distribution
443 and high flux values of above 2000 ppmv/s can also be observed outside the ALTZ and at a distance to the ALTZ boundary
444 (Figure 6 A/C).

445 SO₂ and H₂S in contrast appear spatially stronger confined, and significant flux values can be exclusively observed within the
446 ALTZ (Figure 6 B/D). Values for SO₂ and H₂S inside the ALTZ exceed the outside-ALTZ values by 13 and 15 times. This
447 higher diffuse flux, although at average low concentrations, might promote a surficial process of chemical weathering and
448 surface bleaching, potentially causing the observed color shift from a reddish-oxidized surface toward gray and will be
449 discussed further based on analyses of the geochemical composition of rock samples in Chapter 5.2.

450 Comparing the surface degassing to the observed optical and thermal anomaly pattern (Figure 6 E-G), we see that high values
451 were observed especially in units a or b on the eastern side of the fumarole field, coincident with increased alteration (Type 1
452 and 2) and thermally active surface, followed by other constrained units c - g. However, the strongly bleached and apparently
453 highly altered unit c shows, other than expected, rather small gas fluxes, although its surface temperature is significantly
454 increased with respect to other identified units. This might indicate reduced surface permeability and surface sealing processes
455 and will be discussed in Chapter 5.3.

456 While SO₂ or H₂S flux values for Type 1 and 2 surfaces are increased, only low fluxes were constrained for the Type 3 surface
457 and no flux for the unaltered surface (un in Figure 6 E-G). Note that the central sections of the fumarole field were not sampled
458 due to the close vicinity to HTF and expected high flux values. The data shown here is only representative for the diffuse
459 degassing domain.

460

461 **4.3.2 Mineralogical composition of the alteration gradients**

462 XRD Analysis was performed along two transects A and B, and XRF analysis was performed on samples taken along three
463 transects A - C (Figure 7), crossing postulated alteration gradients.

464 Transect A crosses from the unaltered surface over Type 3 into the Type 1 surface (T3 - T1 boundary in Figure 7) of the highly
465 altered unit c. Transect B is oriented along the HTF on the crater rim in an east-west orientation from Type 1 surface into the
466 LTZ (Type 3). Transect C crosses the eastern fumarole field from the unaltered surface, through the Type 1 and 2 surfaces in
467 unit b, the LTZ (Type 3) on both sides of the HTF, to Type 1 and 2 surfaces, and eventually the unaltered material outside the
468 ALTZ. This transect represents the variability in the rather diffuse degassing regime as no samples close to the HTF were used
469 for the analysis.

470 Results of all samples support local alteration gradients within the ALTZ and show significant changes in the mineralogical
471 and geochemical compositions (Table of XRD results in Appendix F). The dominant mineral phases observed in samples of
472 transects A and B are sanidine, cristobalite, and elemental sulfur (Figure 7). Additionally, most samples contain amorphous
473 material, representing glassy phases typical for volcanic sequences. For comparability, mineralogical concentrations refer to
474 the crystalline phase, while amorphous contents are stated with respect to the total. Note, however, that bulk rock geochemistry
475 refers to both phases and cannot analytically distinguish between amorphous and crystalline.

476 Considering compositional changes along transect A, we observe a high proportion of sanidine feldspar and lesser cristobalite
477 in the relatively unaltered samples (Type 4). With an increasing degree of alteration, we observe a general loss of cristobalite
478 and sanidine while sulfur contents increase (Figure 7). Samples from the unaltered reddish Type 4 surface (sample A1) outside
479 the ALTZ and Type 3 surface (samples A 2/3) inside the ALTZ are similar in composition and show high sanidine and
480 cristobalite contents of 86 - 87% and 13 - 14% in the crystalline part, respectively, yet low to no sulfur contents. These samples
481 were taken in areas of no or only slightly increased surface temperatures of < 22 °C (i.e. < 5 °C above the background). Samples
482 A 4 - 6 are taken in unit c, a complex of high alteration and increased mean surface temperatures of 29 °C (> 10 °C above
483 background). In this strongly altered unit, cristobalite is absent, along with a decrease in sanidine to 60 - 70% relative to the
484 least altered samples and an increase in sulfur contents of up to 20 - 40% in the crystalline portion of the rock sample. However,
485 the amorphous components constitute a high proportion of these sample(s), showing ca. 50% in samples A6 and B1.

486 Samples taken on the upper rim along transect B in the high-temperature fumarole regime contain total sulfur contents of 50
487 to 100%, while cristobalite is absent in these samples. Sample B3, a piece of grayish crust is taken from LTZ 3 (~21 °C, 4 °C
488 above background) in between the high-temperature fumaroles F0 and F5 and contains 100% sulfur, highlighting the
489 precipitation and sealing potential of degassing activity at the surface.

490 Comparing the changes of surface coloration with changes in the mineralogical composition we can constrain no significant
491 effect at the ALTZ boundary, i.e., the transition from unaltered to altered surface (A1 – A 2/3), although the optical effect is
492 major. However, significant compositional changes, e.g. the complete loss of cristobalite and increasing sulfur content are
493 observed at the Type 3 – Type 1 boundary (T3 - T1, blue mark in Fig. 7), coincident with the shift from Type 3 to Type 1
494 surface into unit c.

495 **4.3.3 Bulk geochemical composition of the alteration gradients**

497 For samples without amorphous fraction, bulk geochemical composition correlates reasonably well with mineralogy
498 determined by XRD, assuming ideal stoichiometry. The difference between theoretical bulk composition and true composition
499 is within 10% of the respective element, which we consider a good estimate given sample heterogeneity. Only for sample A5,
500 the high Mn content remains unmatched by XRD analysis. Subtracting the theoretical bulk composition of the crystalline
501 fraction from the true bulk composition, we can thus estimate the chemical composition of the amorphous fraction. The
502 amorphous fraction is similar to the crystalline counterpart mainly composed of SiO₂ and some minor (< 5 wt.%) phases, as

503 well as elevated Mn contents. The high Mn contents were only observed in samples with medium alteration and elevated
504 temperatures, both in samples with and without a significant contribution portion of amorphous material. It is thus likely that
505 Mn is contained in the crystalline phase, yet could not be detected due to the high SiO₂ signals derived from sanidine and
506 amorphous material.

507 The bulk geochemical composition (Figure 7 and data table in Appendix G) agrees with the mineralogical composition. All
508 samples are high in SiO₂ content and, therefore, can be considered to belong to the large silicic-alteration complex earlier
509 described by Fulignati et al. (1999). The samples show a slight variability of SiO₂ between 67 - 82 wt.% and plot on the rhyolite
510 field within the TAS diagram (Middlemost, 1994; not shown here). The amorphous component, typical for rhyolite, consists
511 of mainly SiO₂, with minor amounts of Fe and Al, based on the difference between the theoretical and actual geochemical
512 composition calculated from stoichiometric mineralogy. Three samples also have significant MnO, possibly caused by
513 hydrothermal leaching and precipitation as amorphous crusts. However, the variability of MnO will not be detailed further in
514 this study.

515 Dominant in transect A is the loss of Al₂O₃ from the unaltered Type 4 surface (> 10 wt.%) outside ALTZ to the Type 1 surface
516 of the highly altered unit c (< 0.4 wt.%). Similarly, Fe₂O₃ is decreasing from an average of 1.6 to 0.3 wt.%. The loss of Al₂O₃
517 and Fe₂O₃ is likely related to the alteration of sanidine and the elution of iron- and aluminum-sulfates formed due to the contact
518 with sulfuric gas. The most significant changes occur, similar as observed in the mineralogy, not at the transition from unaltered
519 to altered (ALTZ boundary) but at the T3 - T1 boundary (blue line in Figure 7) at the transition from Type 3 to Type 1 surface.
520 Transect C crosses from the unaltered surface through unit a, the northern LTZ, the southern LTZ, unit b, Type 3 surface, and
521 eventually the unaltered surface. Compositional changes from unaltered (Type 4) to altered (Type 1 and 2) surface of units a
522 and b, here, are minor with relatively stable values for Al₂O₃ (6 - 12%), Fe₂O₃ (1 - 3%), TiO₂ (< 0.5%) and Mn (~0%). At the
523 transition from active units a and b (Type 1 and 2 surface) to the LTZ (Type 3), we observe a significant increase of sulfur
524 content from < 2% to 12 - 40%. However, this increasing sulfur content here is not coincident with the systematically brighter
525 surface color observed for other altered units. LTZ show the same rather dark surface observed for Type 3 surface elsewhere,
526 which is a discrepancy to the effects observed in the western fumarole field and indicates that LTZ have to be considered
527 subject to different surficial processes. This will be discussed in Chapter 5.3.

528 **5 Discussion**

529
530 Various studies have previously explored the geochemistry (e.g. Fulignati et al., 1999), petrology (e.g. De Astis et al., 1997),
531 geophysics (e.g. Revil et al., 2008) and remote sensing signal (e.g. Mannini et al., 2019; Coppola et al., 2022) of the La Fossa
532 crater, Vulcano island. In this study, we combine close-range remote sensing, image analysis, mineralogical and geochemical
533 analyses of rock samples, and the study of the present-day surface degassing of the La Fossa crater and analyse the surface
534 expression of hydrothermal activity. Through this combination of ultra high resolution (< 10 cm) drone image analysis with

535 mineralogical/geochemical analysis, we are able to provide a holistic picture of the surface degassing and hydrothermal
536 alteration pattern, highlighting an aureole-like organisation of the alteration field that distinguishes distinct units that grade
537 from inner high-temperature fumaroles to sealed surfaces (LTZ) and to diffuse degassing areas at a greater distance. An area
538 of approximately 70,000 m², which we have termed the Alteration Zone (ALTZ), outlines the maximum extent of observable
539 alteration effects and highlights that degassing and alteration can be traced well beyond the central high-temperature fumarole
540 activity sites (HTF). The ALTZ is similar to the diffuse flux zone previously identified by Mannini et al. (2019), and is in fact
541 ~60 times larger than the area covered by the high-temperature fumarole domain. However, from the optical data, we observe
542 further variability within this zone expressed in active units a - g, which also coincide with the diffuse thermal activity and
543 cover 25 times the extent of HTF. Here we can further detail the surface structures and activity patterns identified in previous
544 works, (e.g. Harris et al., 2009; Mannini et al., 2019) which divide the active region into a vent flux zone and a diffuse flux
545 zone. In particular, we can further detail the vent flux zone by outlining high-temperature fumarole locations based on high-
546 temperature pixels. We further show that thermal radiation and gas flux of the ALTZ or diffuse flux zone are not uniform but
547 show strong local variability, with high fluxes in identified active units a - g and low fluxes in larger parts of the central
548 fumarole field associated with LTZ (Low-Temperature Zones) or the unaltered regime.

549 Although the structural study is based solely on drone-derived imagery and thermal infrared data, our detailed observations of
550 local activity and alteration gradients are supported by variations in mineralogical and bulk geochemical compositions of
551 representative rock samples. Although we have performed a classification of the image data in this work, already visual
552 observations can show a general shift from reddish to gray surface color, which coincides with areas of increased diffuse gas
553 flow. Such color anomalies can therefore be used as guide in the field. A variability in surface brightness and gray hues
554 coincides with alteration gradients and major active units, and the congruent optical and thermal anomaly pattern indicate the
555 link between surface coloration and degassing-induced alteration processes. This relationship underlines the potential of the
556 presented combination of methods as an efficient first-order site investigation tool for volcanic degassing and alteration
557 systems that can be applied to volcanoes elsewhere.

558

559 **5.1 Alteration Zone (ALTZ) controlled by sulfuric gasses and elution processes**

560 The ALTZ is characterized by a surface color shift from reddish to gray and coincides with higher SO₂/H₂S flux and appears
561 to represent a zone of diffuse acid gas flow (Figure 4). All measurements with a significant flow of sulfuric gas species are
562 from inside the ALTZ, while the flux of CO₂ was high well beyond the ALTZ. We, therefore, suggest the general color shift
563 from reddish to gray to be related to a higher flux of sulfuric gasses, promoting chemical leaching of iron oxides via the
564 reduction of the initially contained iron oxides to iron sulfates, which are strongly soluble in rain or in condensing water vapor
565 and are thus prone to rapid elution. Iron oxide content in our analyzed samples ranges from 1.5% (sample A1) in the unaltered
566 regime, to 1.1 - 1.4% for samples A 2/3, and to 0.3 for samples A 4 - 6 of the highly altered unit c. There is a gradual reduction

567 following the postulated alteration gradient, with the strongest changes along the T3 - T1 boundary (blue line in Figure 7). The
568 1.5% Fe₂O₃ for our rock sample of the unaltered regime is a rather low value and might be related to the fact that the sample
569 was taken very close to the ALTZ boundary. It consists of > 50% amorphous material. Fulignati et al. (1999), who provide a
570 broader sampling database estimated Fe₂O₃ contents of unaltered 1888 - 1890-eruptive products with 2.5 - 6.7%, which reduces
571 to an average value of below 1% in the silicic-alteration regime (Fulignati et al., 1998; Fulignati et al., 1999; Boyce et al.,
572 2007).

573 Further evidence for chemical leaching is found on the crater floor, where deposits form a colored layer resembling the color
574 spectra widely observed on La Fossa, with bright reddish deposits close to the fumarole field resembling fluvial patterns. We
575 believe that the optically anomalous gray surface at Vulcano can generally be used to infer areas of present higher acid gas
576 flux or former discharge of acid gasses. Analyzing the broader area of the central crater region, we can infer multiple other
577 areas where we observe similar changes of colorization that indicate similar argillic or strong silicic alteration effects at the
578 surface. These are located on the southern inner crater, the outer crater rims, the 1988 landslide area (Madonia et al. 2019) and
579 the northern flank towards Vulcano Porto. These zones of strong alteration are indicated in red in Figure 1B or Müller et al.
580 (2021).

581

582 **5.2 Alteration gradients on local scales**

583 With average high SiO₂ contents of > 70%, the sampled areas correspond to the large silicic alteration complex suggested by
584 Fulignati et al. (1999), Azzarini et al. (2001), Boyce et al. (2007), and others. In our study, we show evidence for strong local
585 alteration gradients and structurally important units and spatially constrain them, thus we complement earlier studies.

586 Color shifts observed within the ALTZ associated with units a - g (brightness effects, hues of gray) are likely controlled by the
587 degree of hydrothermal alteration, secondary mineral formation, and especially sulfur content in the respective surface samples.
588 Coincident with characteristic changes in the surface coloration from Type 4 towards stronger bleached surfaces of Type 1,
589 we observe a relative decrease of the initial mineral and element composition and a simultaneous increase in sulfur content for
590 most of the obtained samples (Figure 7). While sulfur content in Type 1 surface ranges from 6 to 31%, for Type 2 it is already
591 below 2%, and for the unaltered fraction, it is below 0.2%. We can, therefore, confirm a general link between alteration
592 gradients, sulfur contents, and surface brightness (or surface types) in our remote sensing data (Figure 8).

593 An exception from this trend are sulfur contents of the Type 3 surface. Here we observe two distinct clusters (Figure 8), one
594 with values below 0.5% and one with extraordinarily high sulfur contents of 12 to > 60%, both showing a similar surface
595 coloration. All Type 3 samples with high sulfur contents are exclusively taken from LTZ. This strong discrepancy of sulfur
596 content and surface coloration within the Low-Temperature Zones suggests next to alteration gradients also surficial or shallow
597 processes of mineral deposition and formation of sulfur-rich encrustations that form sealed surfaces, especially in the near field
598 of fumaroles. The low temperatures observed within LTZ and the limited surface degassing highlight the efficiency of such
599 sealing processes. So far we can not distinguish LTZ from Type 3 surfaces in our optical data (Figure 8). A distinction,

600 however, would be beneficial as it would provide a method allowing for the precise spatial constraint of sealed surfaces from
601 simple UAS-derived RGB imagery.

602 The intensity of optical and thermal effects and associated changes in mineralogical and chemical composition, and degassing
603 are not always equally significant. Although the general shift from unaltered surface to altered surface (ALTZ boundary, shift
604 reddish to gray) is a major criterion for the identification of degassing and alteration extent in our data, the associated changes
605 in compositions are minor (Figure 9). The larger changes are observed within the ALTZ at the T3 - T1 boundary (Figure 7).
606 Here we observe a sudden decrease in the initial mineral and bulk geochemical composition and an increasing sulfur content.
607 We interpret the rather low changes at the transition from unaltered to altered at the ALTZ boundary to be related to rather
608 weak or surficial alteration effects. The size of obtained samples was on the order of ~ 2000 cm², including the surficial part,
609 but extends down to ca. 10 cm depth. This way, it was not possible to trace mineralogical or geochemical changes at the surface
610 only. The samples obtained at the T3 - T1 boundary, on the other hand, show strong changes and reveal the general systematics
611 of alteration effects, especially those samples taken in unit c, which might be considered one of the strongest alteration end
612 members of the central crater region.

613 The identified surface patterns with respect to alteration gradients and structural units result from long-term evolution.
614 However, some features may be subject to rapid changes. During the volcanic crisis in 2021, we observed, for instance, the
615 formation of a new fumarole complex, which will locally change the composition, sulfur content, and surface type considered
616 (cf. Figure 11), as is the case with sulfur deposits at the surface that can change quickly due to rainfall.

617

618 **5.3 Heat budget - evidence for diffuse activity and surface sealing**

619 Heat budgets on Vulcano have been studied earlier by e.g. ground-based surveys or satellite data (Chiodini et al., 2005; Harris
620 et al., 2009), providing a range of estimates of thermal emissions (Mannini et al., 2019; Silvestri et al., 2019; Coppola et al.,
621 2022). We compare our results to those using a remote sensing approach. Mannini et al. (2019) outlined a diffuse flux zone,
622 which is comparable to the ALTZ defined by us. Further, they divided this zone into a diffuse flux zone and a vent flux zone
623 and estimated the thermal radiation.

624 We outlined the surface structure of the degassing and alteration system (simplified in Figure 10 and detailed views of the
625 different alteration and thermal units in Appendix C) based on the detection and classification of optical and thermal anomalies
626 supported by additional mineralogical, geochemical, and degassing information, and spatially constrained high-temperature
627 fumaroles (HTF), major diffuse active units a - g, and Low-Temperature Zones (LTZ). We quantified their importance for the
628 degassing and alteration system by calculating their thermal energy release according to the Boltzmann Law (Eq2 and Figure
629 10) for both, anomalies with $T > 22$ °C, and identified units based on a spatial constraint, also including values < 22 °C.
630 Therefore our identified structure differs from the vent flux and diffuse flux zone shown by Mannini et al. (2019).

631 High-temperature fumaroles in our study have average radiant exitance values of 82 W/m² but can only account for 28% of
632 the total emitted thermal energy (calculations based on pixels with $T > 22$ °C and a corrected background of $T = 16.71$ °C).

633 Note that when considering pixels with $T > 40$ °C (as outlined by red patches in Figure 4D) the cumulative radiation of HTF
634 would decrease to 0.2 MW only and the radiant exitance would increase to 242 W/m². The rest is released by the diffuse
635 degassing part of the system. Although a direct comparison may be difficult, due to different outlines chosen for the respective
636 flux zones, different sensor systems, and different background correction values, our cumulative radiation (R_{cum} in Figure
637 10) for the HTF is comparable to those of Mannini et al. (2019). These authors suggested a vent zone heat flux of 0.35-0.96
638 MW. Our estimate was ~1 MW, of which 0.5 MW are contributed by the high-temperature fumarole vents and 0.52 MW by
639 unit c. This is also in accordance with the findings of Coppola et al. (2022), who estimate a similar vent zone flux from VIIRS
640 imaging bands.

641 However, the contribution of the diffuse thermal regime approximated by us is lower compared to estimates in other studies
642 (e.g Mannini et al., 2019), which place the contribution of the diffuse flux zone (comparable to our ALTZ) on the order of
643 90% of the total flux. This is likely related to the fact that we did not estimate the flux of the ALTZ in total, but of multiple
644 larger anomaly units within the ALTZ that have apparent structural importance for the degassing system and contribute ~50%
645 to the total flux. For future studies, a distinction into 3 different thermal regimes, a vent flux / high-temperature fumarole zone,
646 diffuse active units (like a-g shown in this study), and a broader low-temperature anomaly field (diffuse flux zone/ ALTZ)
647 may be recommended to better resolve close range thermal-infrared remote sensing information with data from satellite-based
648 studies.

649 Regarding the heat budget estimated by us, the most dominant diffuse unit in terms of thermal energy release is unit c. It has
650 the second-highest average radiant exitance of 76 W/m² and exceeds, with 29% of the total thermal radiation, the cumulative
651 radiation of the HTF. Unit c is not only a highly altered complex with the strongest bleached surface and increased surface
652 temperatures, there is also a discrepancy to the current degassing activity. Relative gas flux values measured within unit c are
653 lower than observed for units a and b, for instance. This phenomenon might be a consequence of the permeability reduction or
654 sealing processes due to the more advanced hydrothermal alteration (cf. Heap et al. 2019). This proposition is supported by
655 the strongest changes in mineralogical and bulk geochemical composition observed in our samples, implying mineral (re-)
656 precipitation is a major process in this particular unit.

657 Diffuse aureoles (unit a/b) on the eastern side of the fumarole field cover several thousand m² each, more than the area covered
658 by HTF. The diffuse aureoles contribute 6 to 7% each to the total thermal energy release, equivalent to 25% of the energy
659 emitted in the high-temperature zone (HTF + unit c). Their bleached surface, increased surface temperatures (Figure 4), and
660 higher gas flux values (Figure 6 E-G) highlight their importance for the surface gas-drainage capability. However,
661 mineralogical and bulk-chemical data suggests that the degree of alteration is less in these units, compared to unit c. This
662 observation suggests that these sections are younger and therefore less altered and highlights their importance for the present-
663 day degassing system.

664 Units d and e are large diffuse degassing domains of the western fumarole field of which unit d is a part of the thermal aureole
665 surrounding F0 and unit e is a ~200 m long branched anomaly, located rim parallel west of F0. Both have a similar contribution
666 to the total thermal energy release as units a and b. Unit d is separated from F0 by a Low-Temperature Zone (LTZ 3). The

667 transition from LTZ 3 to unit d is sudden and accompanied by a temperature jump of ~20 °C. The difference in the average
668 temperature between unit d and LTZ 3 is on the order of 5 °C. Also here we observe apparent surface sealing for the whole
669 central fumarole field. Unit f, the northern section of the F0 aureole, and anomalies in the area north of the fumarole field (unit
670 g) have a minor contribution.

671 The Low-Temperature Zones (LTZ) 1 - 3, which separate diffuse aureoles from the HTF, have a Type 3 surface coloration,
672 significantly lower temperatures and radiant flux and exitance values than the neighboring aureole regions, what indicates
673 processes of surface sealing. Indeed, no gas flux could be constrained for the LTZ of the eastern fumarole field. From field
674 observations and lab analyses (Figure 7), we constrained the LTZ as strong, sulfur-rich surface complexes that effectively seal
675 the surface and inhibit gas escape. The depth of these sealed complexes can not be constrained by our data, but we can
676 approximate the spatial extent. Considering only the 3 LTZs of the central and eastern fumarole field, they cover a total area
677 of ~12,000 m², which is a significant fraction of the ALTZ. In other words, ~20% of the surface of the ALTZ is apparently
678 sealed, which forces lateral gas flow to the aureole regions. This was proven by observations during the 2021 volcanic crisis
679 at La Fossa. While at fumarole sites and diffuse active units like units a and b showed an increase in mean temperatures and
680 thermal energy release, the radiation within LTZ remained stable and low, highlighting the efficiency of the proposed seal.
681 This was observed for all central LTZs, and is exemplified in a cross-section through the eastern fumarole field section in
682 Figure 11D.

683 **6 Conclusion**

684 Our investigation of the fumarole field of the La Fossa cone allowed us to constrain the degassing and alteration structure,
685 define major, so far undescribed units of activity, and quantify their importance for the degassing system. Such high-resolution
686 studies can greatly contribute to the understanding of structural architecture and add to our understanding of the intrinsic
687 complexities of fumarole fields. This realisation has implications for hydrothermal alteration studies, particularly for the
688 identification of local variability, since local variations are frequently associated with mechanical, chemical, and permeability
689 contrasts. The recognition of such contrasts is of use for an improved assessment of volcanic and degassing activity, but also
690 possibly for other hazard aspects, such as e.g. stability assessments. We anticipate that combined remote sensing and
691 petrological studies will prove beneficial for pre-site reconnaissance surveys for hydrothermal energy exploration, the
692 detection of sampling locations for alteration-related studies, and, importantly, for hazard monitoring of volcanic crater areas
693 and associated risk assessment.

694

695 **7 Tables**

696 **Table 1:** Overview of the processed data sets that were used for the following analyses. From the optical data, an orthomosaic
697 and DEM were generated covering 3.74 km² with pixel resolutions of 8.6 x 8.6 to 17.3 x 17.3 cm. From the high-altitude
698 infrared overflight, an infrared mosaic was acquired covering 3.23 km² with 38 x 38 cm resolution. All data sets cover the
699 complete central section of the La Fossa cone.

700

Data set	Acquisition date	Pixel resolution in cm	Coverage in km ²	Point density in p/m ²
2019 orthomosaic	14.11.2019	8.6 x 8.6	3.74	135.20
2019 DEM	14.11.2019	17.3 x 17.3	3.74	33.41
2018 IR mosaic	15.11.2018	38 x 38	3.23	5.64

701

702

703

704

705

706

707

708

709

710

711

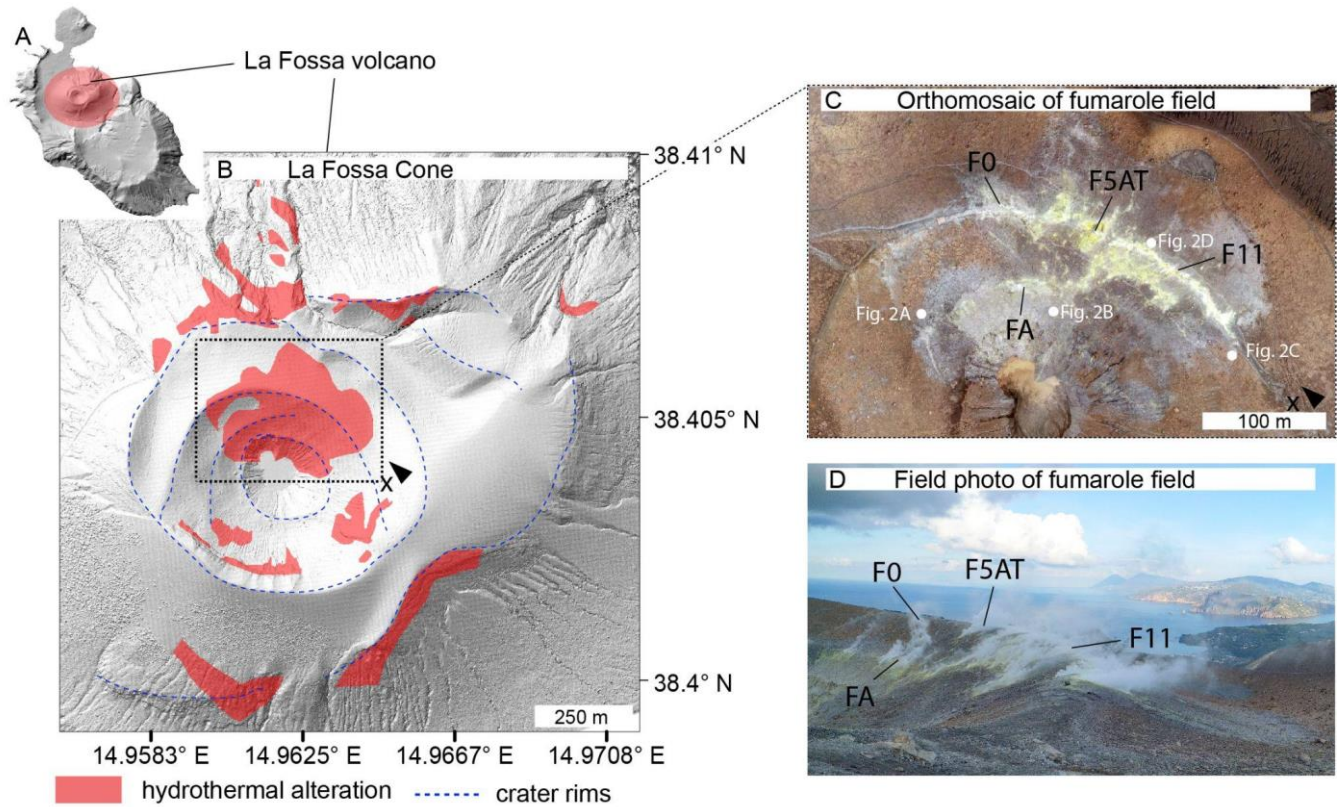
712

713

714

715

716



720 Figure 1: Overview of the degassing sites at La Fossa cone, Vulcano Island (Italy). A) Vulcano Island as a shaded relief map.

721 The red circle indicates the location of the La Fossa cone. B) Central summit area of the La Fossa Cone. Blue dashed lines

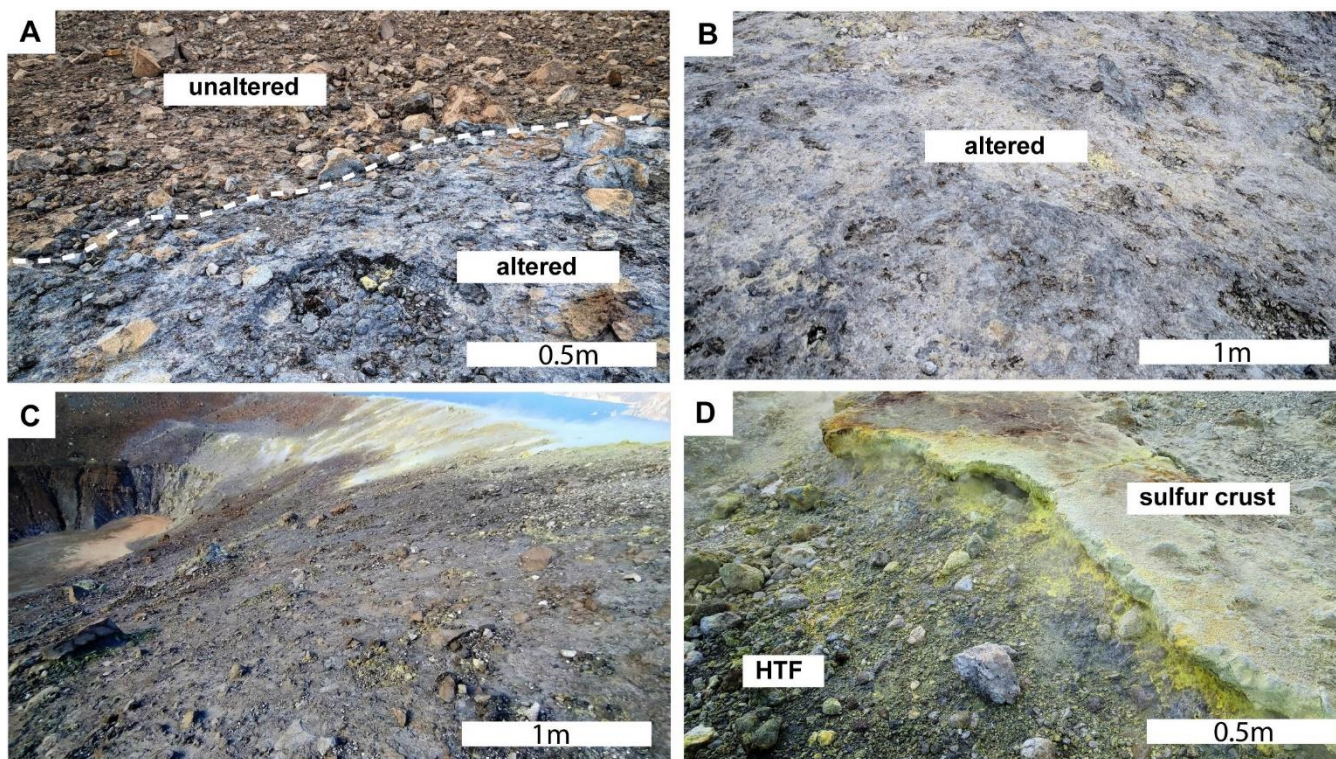
722 indicate crater rims from different eruptive episodes. Areas of degassing and hydrothermal alteration are highlighted in red

723 following Müller et al. (2021). The dashed box outlines the most prominent center of degassing and alteration, the high-

724 temperature fumarole field. C) Birds-eye view of the high-temperature fumarole field with prominent fumaroles F0, F5AT,

725 F11 and FA marked. The locations of field photographs of Figure 2 are indicated by white dots. D) Field photo of the fumarole

726 field. Location and viewing direction are indicated by an x and an arrow (B/C).



728

729 Figure 2. Different surface types and colorations at the La Fossa cone. A) Transition from unaltered to altered bleached
 730 surface. B) Intensely altered and bleached surface. C) View from the east onto sealed surfaces. D) High-temperature fumarole
 731 (HTF) and deposited sulfur crust.

732

733

734

735

736

737

738

739

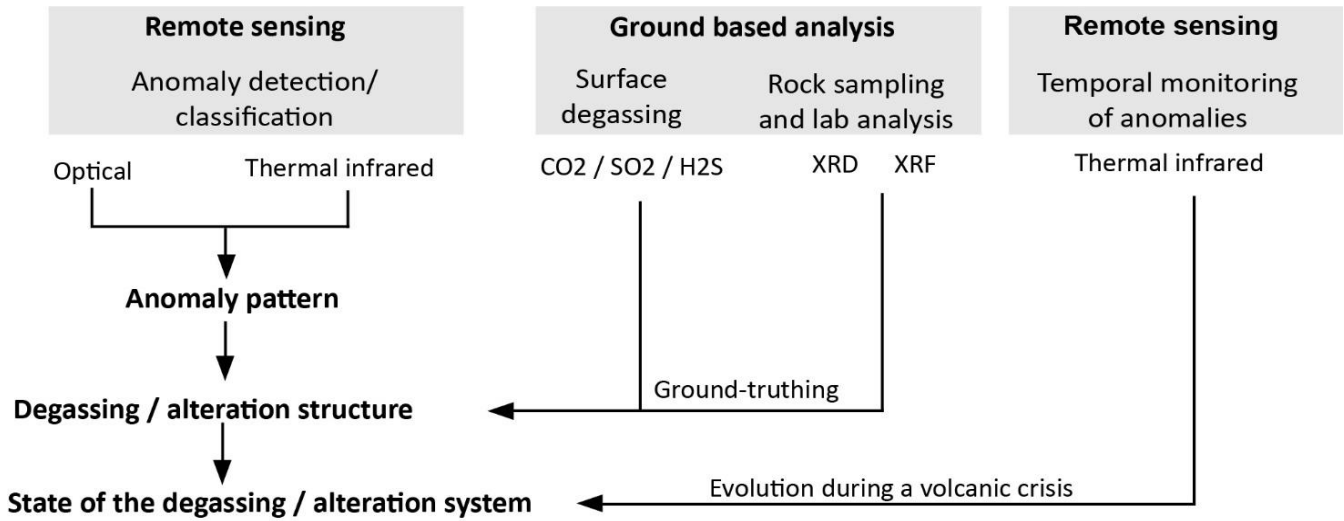
740

741

742

743

744



746

747

748

749

750

751

752

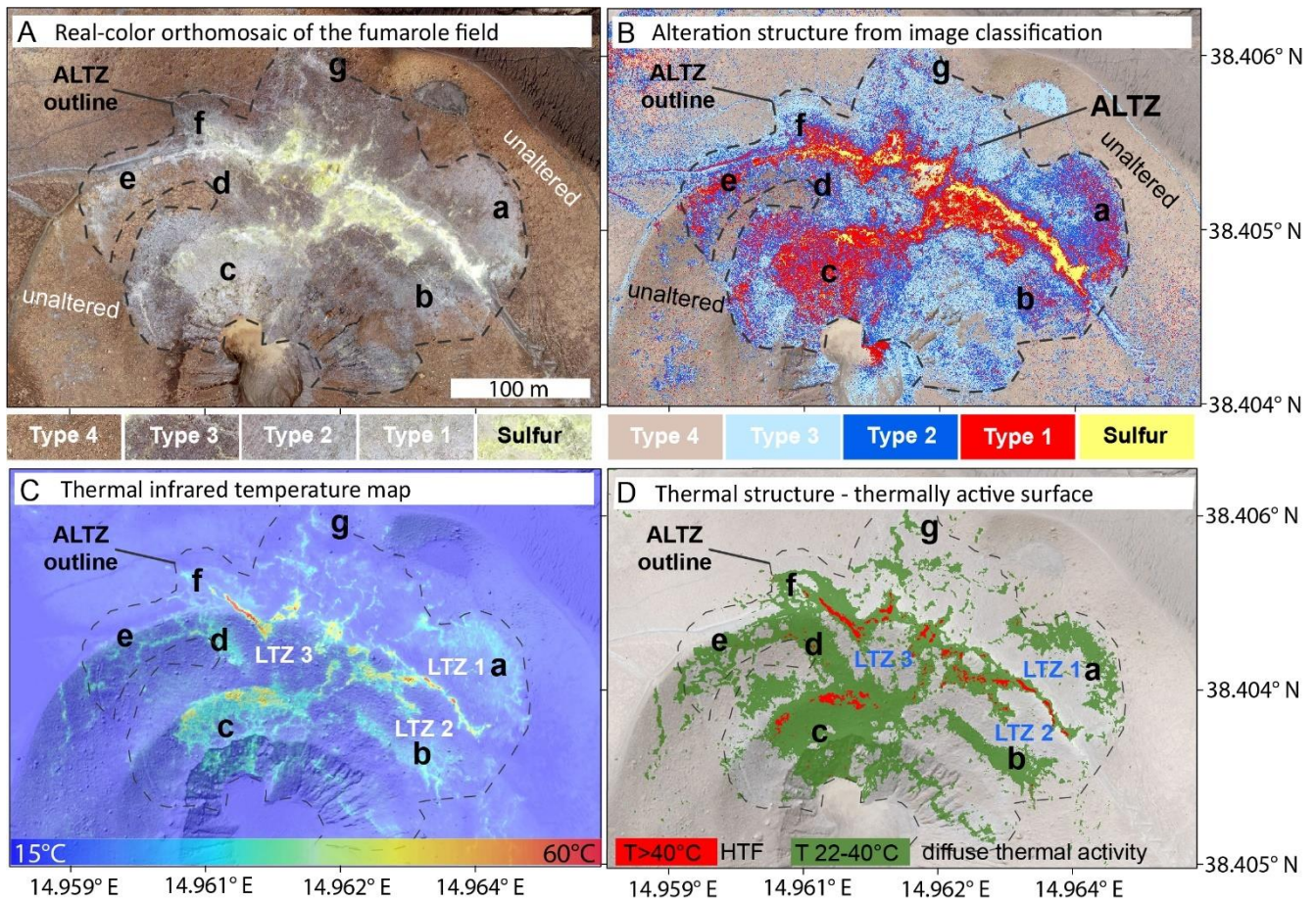
753

754

755

756

Figure 3: Overview of the general workflow used for this study. An anomaly detection from optical and thermal infrared remote sensing data allows us to reveal the anomaly pattern and infer the surface structure of the degassing and alteration system. To validate the observed structure, the remote sensing study was complemented by surface degassing measurements revealing the present-day degassing pattern, and by X-ray diffraction (XRD) and X-ray fluorescence (XRF) analysis of selected rock samples to prove different alteration units based on changes in mineralogical and bulk-chemical composition. Continuous monitoring by high-resolution thermal remote sensing data allows to record dynamics within the system and to draw conclusions about the general condition of the degassing/alteration units, e.g. with regard to alteration-related processes like surface sealing.



757

758

759

760

761

762

763

764

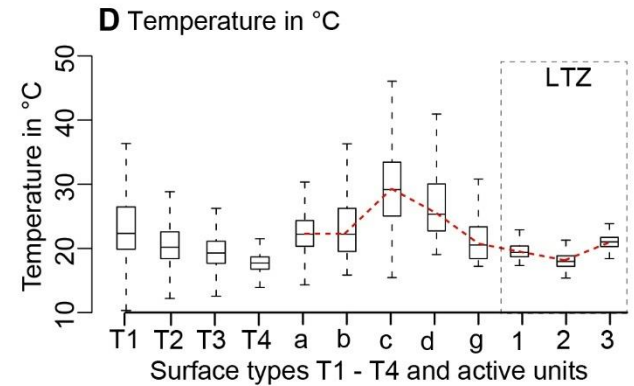
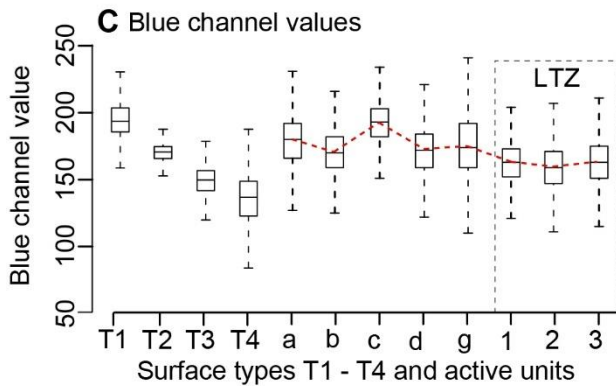
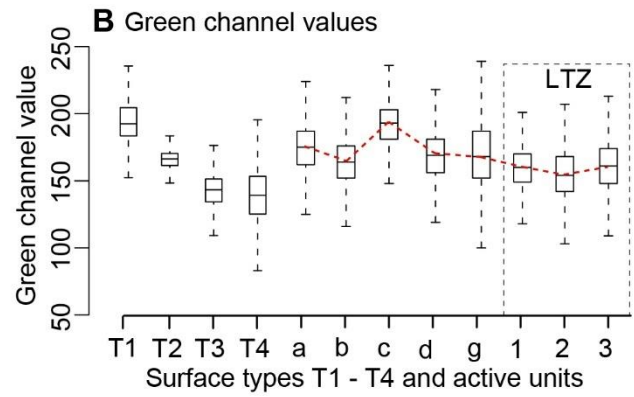
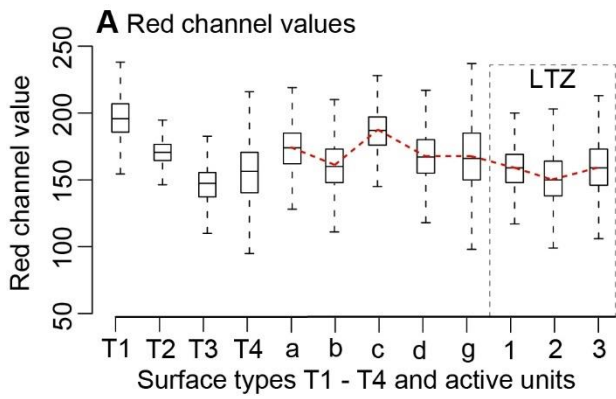
765

766

767

768

Figure 4: Alteration structure of the La Fossa fumarole field. A) True color image of the high-temperature fumarole field with color samples of the surface types 1 - 4 and sulfur at the bottom of Fig. A. B) Alteration structure of the fumarole field as revealed by PCA and image classification, represented by the classified surface types 1 - 4 and sulfur at the bottom of Fig. B. C) Thermal infrared temperature map of the fumarole field. D) Simplified thermal structure of the fumarole field highlighting high-temperature fumarole location in red ($T > 40\text{ }^{\circ}\text{C}$) and diffuse thermal activity in green ($T = 22 - 40\text{ }^{\circ}\text{C}$). The dashed line labeled ALTZ outline demarks the boundary of visible optical effects at the surface and is referred to by us as ALTZ (Alteration Zone). The labels a-g demark notable large-scale anomaly units that can be observed in both, the optical data and thermal data. LTZ 1 - 3 demark Low-Temperature Zones that separate the high-temperature fumaroles and diffuse active units and cover significant parts of the central fumarole field. Note that the contrast of the background image has been reduced for highlighting in Subfigures B and D.



769

770

771

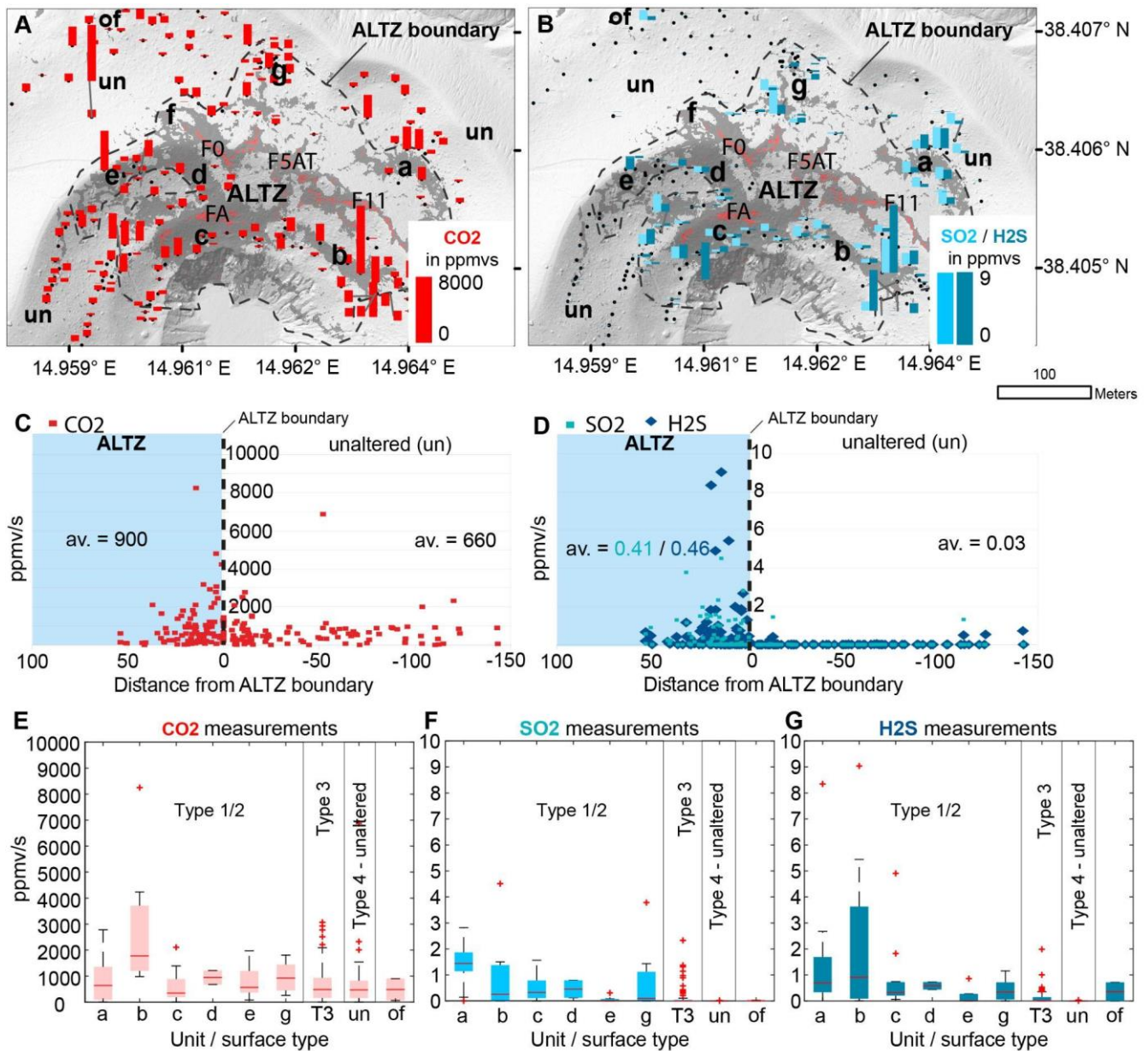
772

773

774

775

Figure 5: Boxplots of RGB color value- and temperature distributions observed for the different surface types 1 - 4 (T1 - T4), identified active units a - g, and associated Low-Temperature Zones LTZ 1 - 3. Surface types and locations of identified units are depicted in Figure 4B/D. A) Red channel value distribution. B) Green channel value distribution. C) Blue channel value distribution. D) Temperature value distribution. Values are based on an analysis of 6.8 million pixels within the ALTZ. Both, the optical (Figure A - C) and thermal (Figure D) value distributions show similarities with generally decreasing values from the T1 - T4 surface, a peak in unit c, and low values for LTZ 1 - 3.



776

777

778

779

780

781

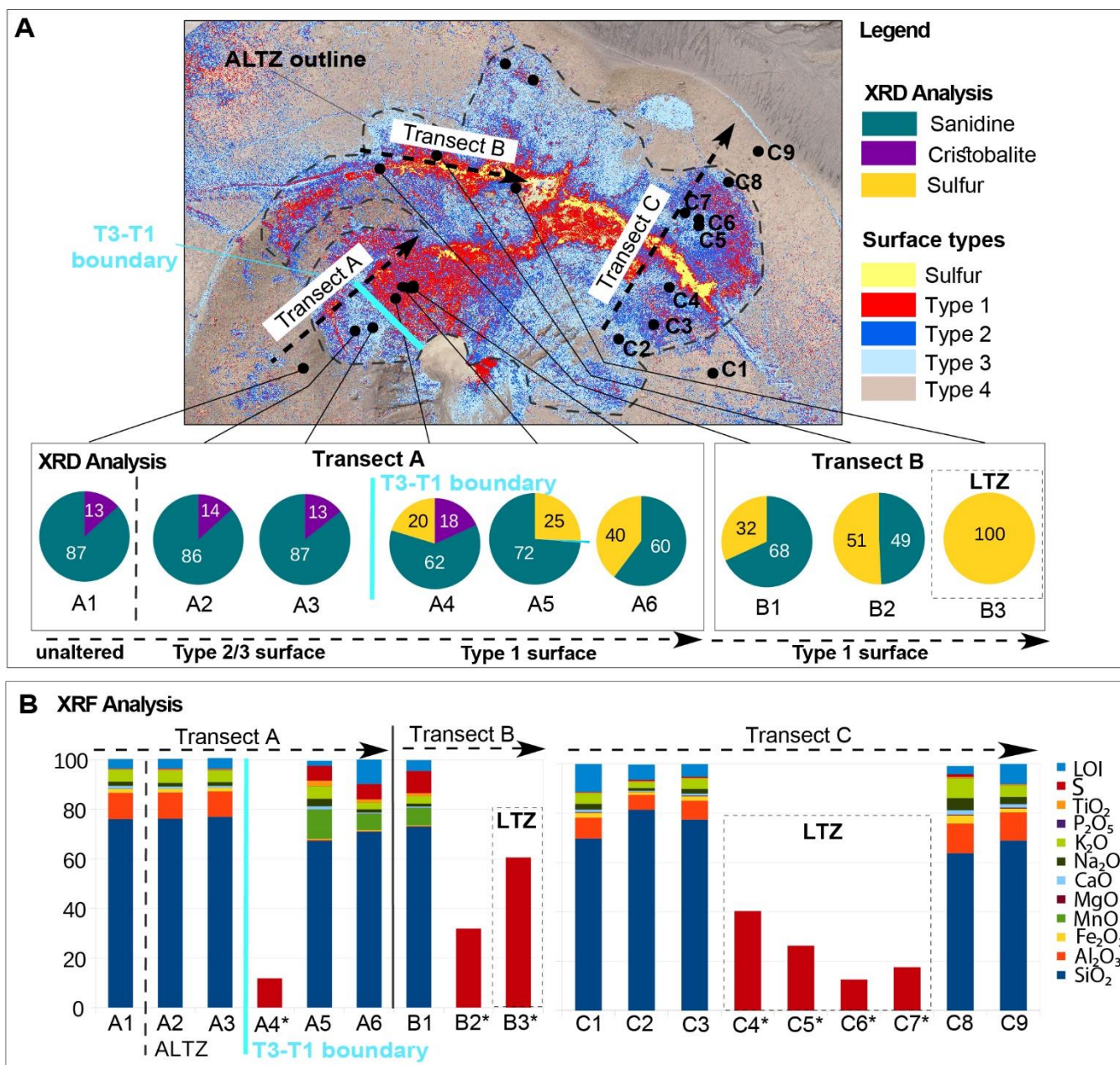
782

783

Figure 6: A/B) Spatial distribution and flux values for CO_2 (red bars in A), SO_2 (light blue bars in B), and H_2S (turquoise bars in B) in a map view for 200 measurement points. Each bar represents a relative flux value at a measurement location. In case no flux was detectable, the respective location is marked with a black dot only. The dashed line highlights the ALTZ (Alteration Zone) boundary. Dark grey features in the background highlight the thermally active surface (compare Figure 2D). Labels F0, F5AT, F11, and FA mark prominent high-temperature fumaroles. The labels a - g mark notable large-scale anomaly units. C/D) Flux values are plotted by distance to the ALTZ boundary (dashed line). Measurement points within the ALTZ are represented by positive distances from the ALTZ boundary (highlighted by blue background) and measurements outside the

784 ALTZ by negative distances (unaltered). A generally higher flux is observed within the ALTZ, but while CO₂ is also abundant
785 outside the ALTZ, significant SO₂ and H₂S fluxes were observed exclusively within the ALTZ, especially on the outer edges
786 and associated with units a - g. The averaged flux values (av) are depicted in the respective sections of C and D. E-G) Relative
787 flux values of identified units (a - g), Type 3 surface (T3), the unaltered surface (un), and fumaroles on the northern rim at a
788 distance (of) highlight the spatial variation of different gas species with high flux values for units a and b, lower flux values
789 for e.g. unit c and generally lower flux of sulfuric gas species in the unaltered regime outside the ALTZ.

790



791

792

793

794

795

796

797

798

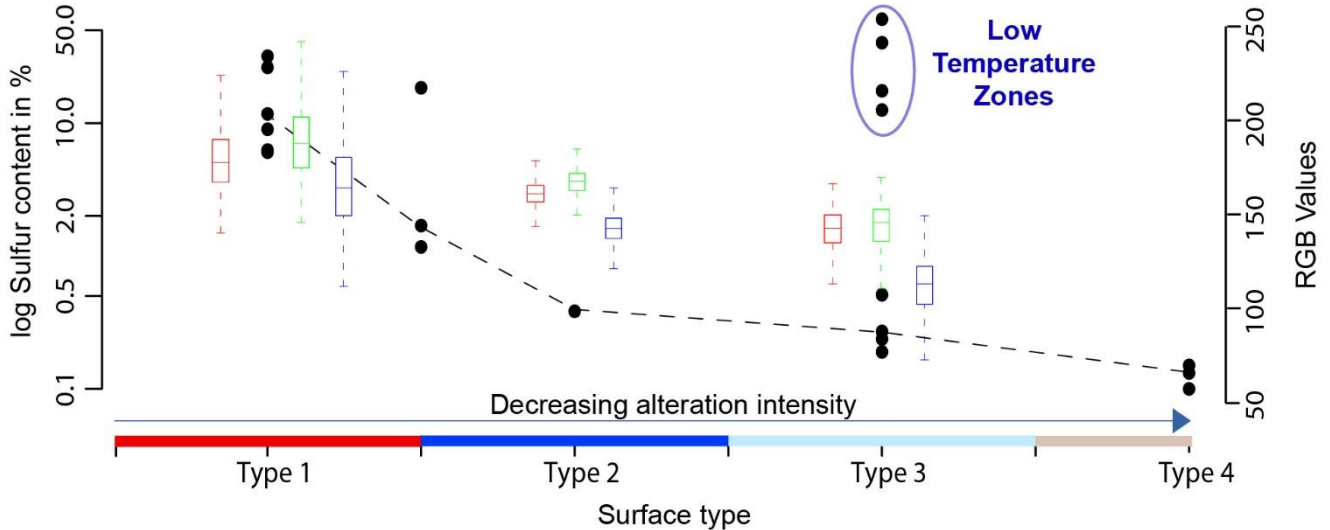
799

Figure 7: Mineral and bulk chemical composition of rock samples along 3 transects A - C, crosscutting alteration gradients, and structural units. A) Overview map with defined surface types T 1 - 4, highlighting the area with visible optical changes at the surface, referred to as ALTZ (Alteration Zone, marked by a dashed line). The three transects A - C were placed so that they crosscut prominent units. Mineralogical compositions from XRD (X-ray diffraction) are depicted by circular plots at the bottom of Fig. A. B) Bulk chemical composition from XRF (X-ray fluorescence) analysis of transects A - C. Transect A/B) With increasing alteration intensity we observe a relative decrease of the initial mineral phases sanidine and cristobalite whereas the sulfur content increases. Note that the mineral composition in this figure is normalized to 100% non-amorphous minerals. In the chemical composition, we observe a significant decrease of Al₂O₃ and Fe₂O₃ but an increase of MnO, TiO₂,

800 and S with increasing alteration, especially at the Type3 - Type1 (T3 - T1) boundary marked in light blue. For transect C we
 801 observe a dominant increase of S (17 - 40%) for samples taken within the LTZ (Low-Temperature Zone). Compared to other
 802 transects, changes in Al₂O₃, Fe₂O₃, TiO₂, and MnO are less significant. For samples marked with an asterisk (*) XRF results
 803 are not available. No XRD results are available for transect C.

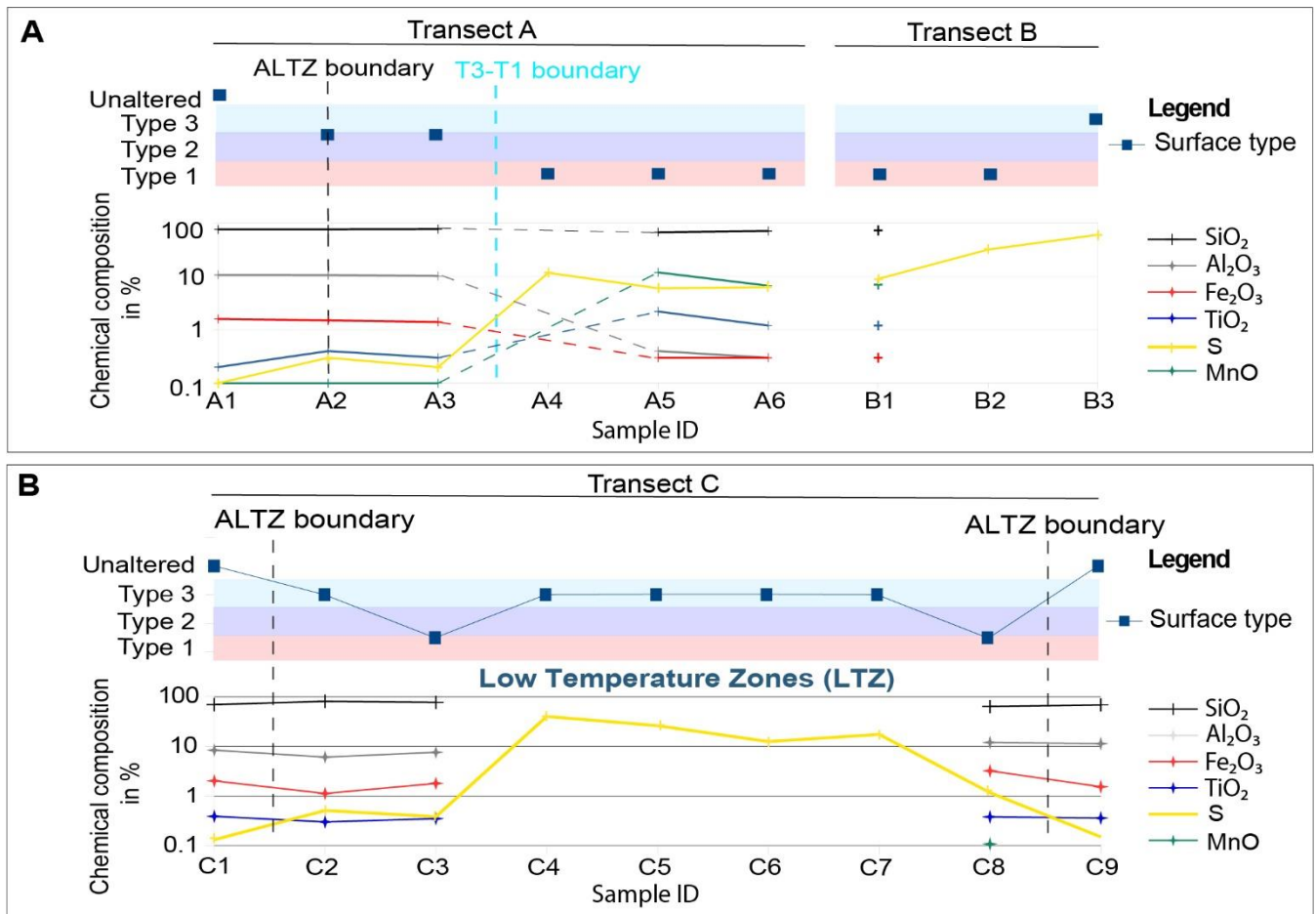
804

805



806

807 Figure 8: Relation of inferred surface type (T 1 - 4) and sulfur content of rock samples taken in the respective surface T 1 - 4.
 808 Black dots mark the sulfur contents of rock samples and are shown on a log scale versus the surface type from which the
 809 sample was taken, labelled by Type 1 - 4 on the x-axis and demarked with boxes using the same color code as throughout the
 810 manuscript. With decreasing alteration from Type 1 surface to Type 4 surface, we see a significant decrease of sulfur content
 811 from up to 100% for Type 1 to < 1% for Type 4 surface. The black dashed line illustrates this. An exemption is the Type 3
 812 surface where we observe two distinct clusters, one with low sulfur values and one with exceptionally high sulfur values. These
 813 high sulfur values belong to samples taken in the LTZ (Low-Temperature Zones), which separate fumaroles from the larger
 814 diffuse active units a and b (compare Figure 4) for instance. These samples indicate that LTZ represent sulfur-rich crusts that
 815 block heat and gas flux from the surface. The colored boxplots show the distribution of RGB values for the respective surface
 816 Type 1 - 4, showing a similar trend of decreasing values. Red boxplots represent the red value, blue and green the respective
 817 blue and green channel values of the image. The coincidence between both indicates a direct relation or control of sulfur onto
 818 the surface colorization.



819

820

821

822

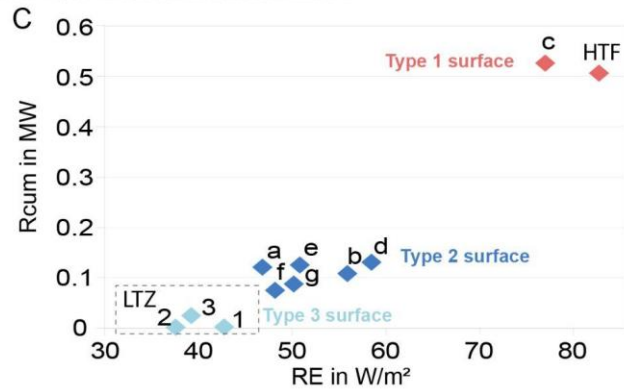
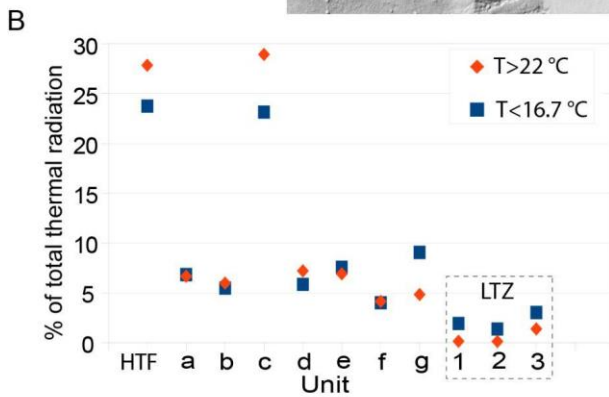
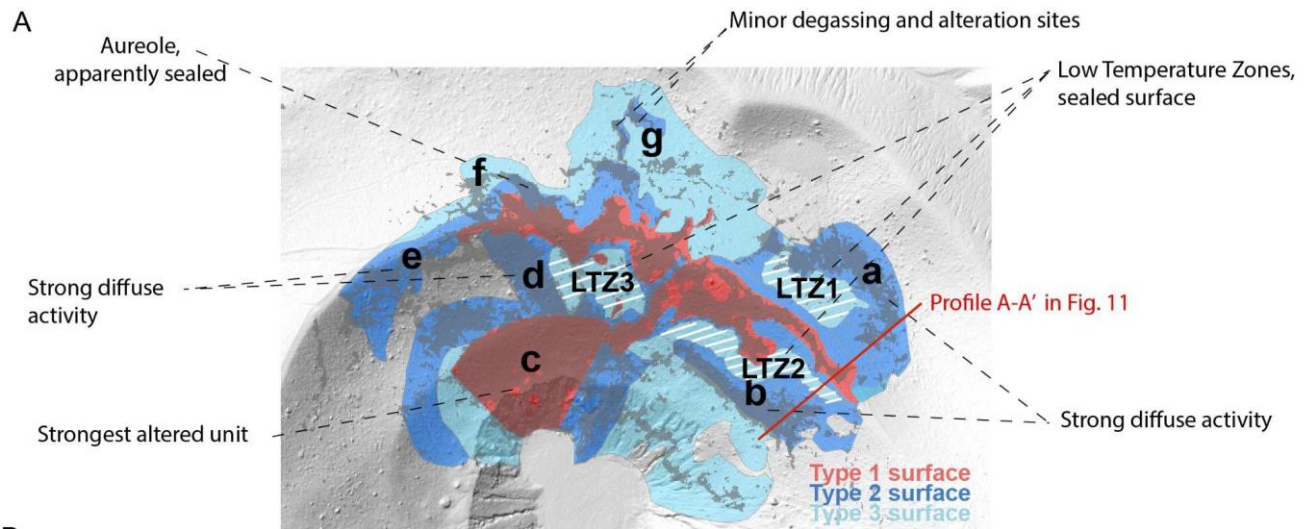
823

824

825

826

Figure 9: Changes of surface type and bulk-chemical composition observed along transects A - C. Locations for the transects and sample ID are shown in Figure 7. A) With increasing alteration from Type 4 to Type 1 surface we observe a reduction of Fe₂O₃ and Al₂O₃ and an increase in sulfur. While changes observed at the ALTZ boundary (black dashed line) are only minor, strong changes are observed at the Type 3 - Type 1 boundary (T3 - T1, blue dashed line). Sulfur contents in transect B were so high that XRF results were only available for sample B1. B) Changes observed in the eastern fumarole field along transect C are less significant, with the exception of extraordinarily high sulfur content for Type 3 samples collected in the LTZ.



827

828

Figure 10: Anatomy of the fumarole field. A) Simplified structure of the fumarole field highlighting surface types and

829

structural units of increased diffuse activity (a-g) or areas of apparent surface sealing (LTZ 1 - 3 marked by white lines). B)

830

Contribution to the total thermal radiation in % for HTF (high-temperature fumaroles), units a - g, and LTZ 1 - 3 (Low-

831

Temperature Zones) considering pixels with $T < 22\text{ °C}$ (blue) and for identified units based on a spatial constraint and pixel

832

temperatures $> 22\text{ °C}$ (orange). C) Radiant exitance (RE) in W/m^2 and cumulative radiation (Rcum) in MW. Rcum is the

833

cumulated background corrected radiant exitance (Equation 2 in the method section) of all pixels associated with the respective

834

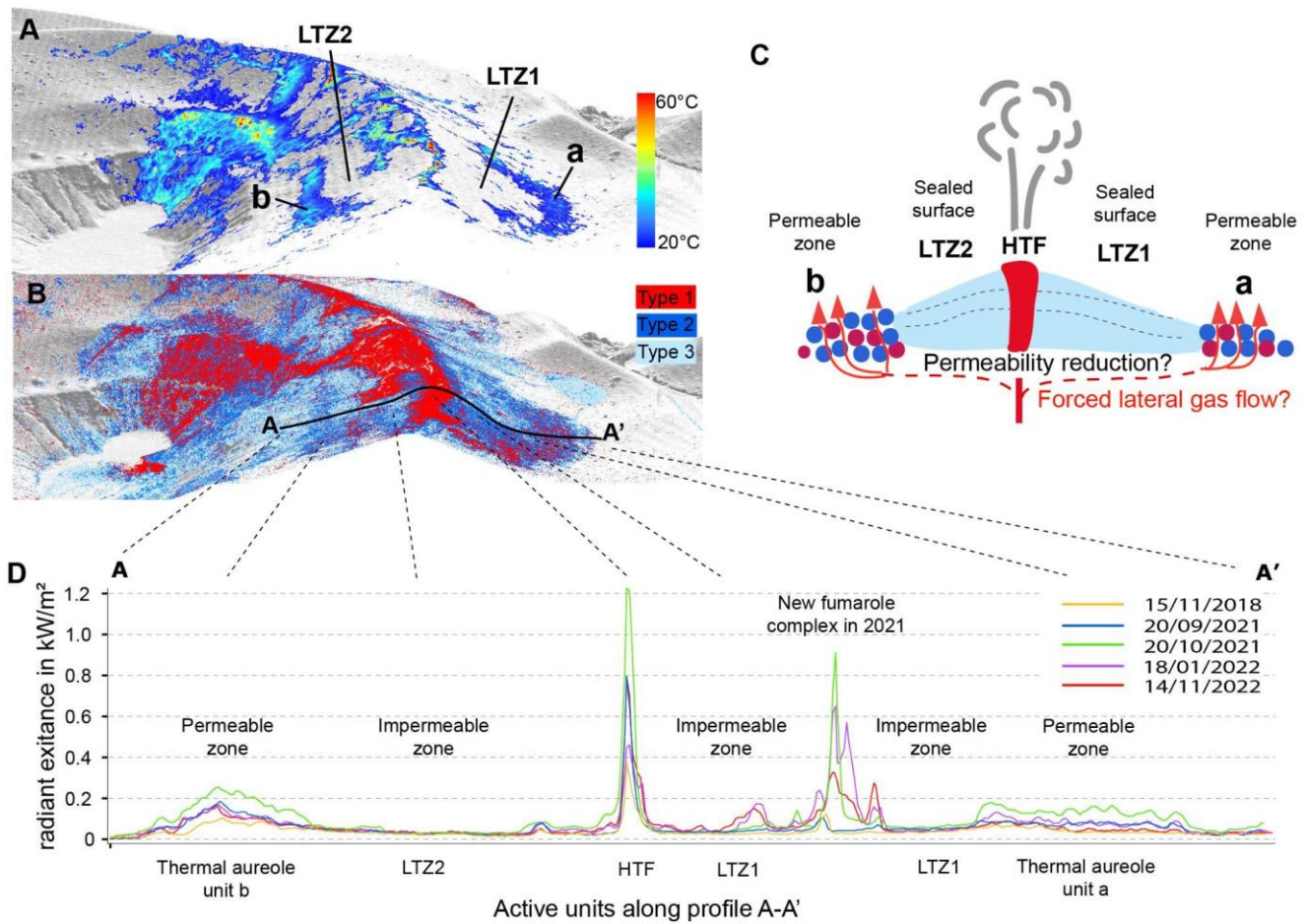
active unit. Note that for Rcum only pixels with $T > 22\text{ °C}$ were used. We can clearly distinguish different thermal regimes

835

that are also coincident with surface types identified in the optical data.

836

837



838

839 Figure 11: Cross section of the eastern fumarole field along Profile A - A' (location see Fig.10) highlighting the structural
 840 setup from high-temperature fumaroles in the center to LTZ and diffuse aureoles at a distance. A) Thermal structure along the
 841 cross-section. B) Alteration structure along the cross-section. C) Schematic sketch along cross-section A-A', highlighting the
 842 central LTZ that might be controlled by surface sealing processes or deeper effects of permeability reduction in the vicinity to
 843 the high-temperature fumaroles due to long-term gas-rock interaction and alteration processes. D) Evolution of thermal
 844 radiation values during a volcanic crisis. While thermal radiation at fumaroles and aureoles increased, radiation values of LTZ
 845 remained unchanged, therefore highlighting the efficiency of surface sealing.

846

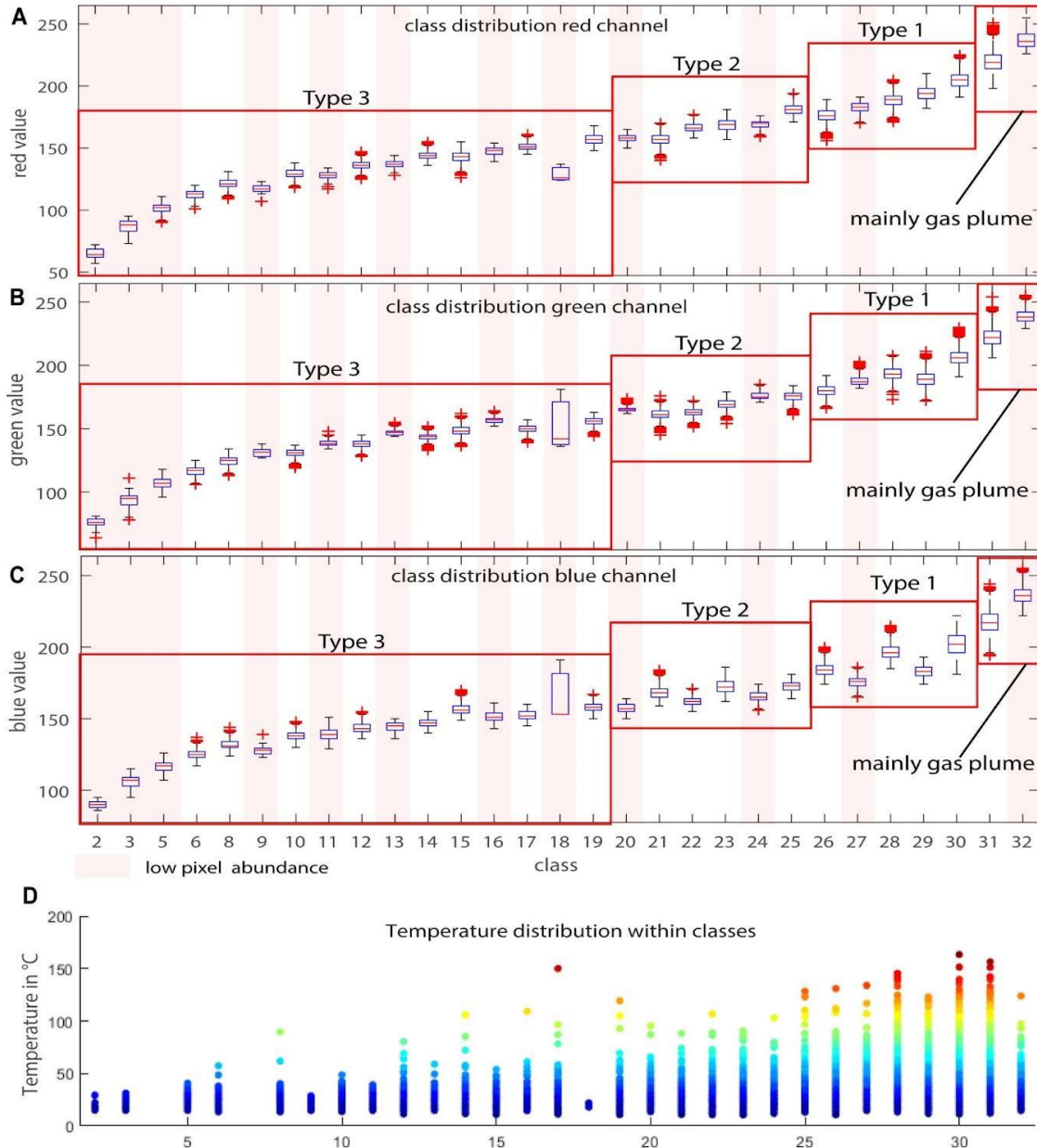
847

848

849

850

851



854

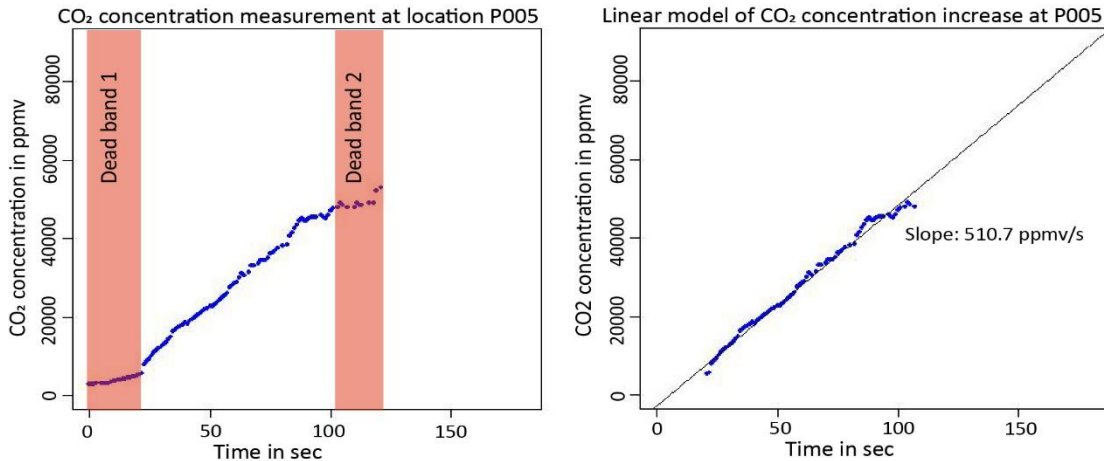
855

856 Figure A1: Boxplots of RGB value distribution for the defined surface Types 1 - 3. Classes (unsupervised classification 32
 857 classes) marked with the transparent red bar only have minor pixel abundances. Red boxes depict the spectral range of Type 1
 858 - 3 surfaces. Class 31 and 32 are mainly associated with the fumarole steam plume.

859

860

861 Appendix B: Gas measurement procedure - simplified accumulation chamber approach



862

863 *Figure B1: CO₂ measurement at location P005, here shown representative for all measurement points. Dead bands at the*
864 *beginning and end of the measurement were removed and the intensity of gas flux was characterized by linear regression*
865 *through the constantly ascending part of the graph. The slopes of the linear model allow a relative comparison of single*
866 *measurement points.*

867

868 To compare the observations from remote sensing to present-day surface degassing, gas-measurement campaigns were
869 performed in September 2021 and November 2022. The surface degassing was measured at 200 points within the northern part
870 of the La Fossa cone (Figure 6 in the main manuscript), in a simplified Multigas accumulation chamber approach.

871 The simplified accumulation chamber consists of the measurement unit, a Dräger X-am 8000, coupled to a 10.3 cm diameter
872 and 16.5 cm long plastic chamber by a 116 cm long tube with an inner diameter of 0.5 cm, resembling a simplified
873 accumulation chamber. The plastic chamber has a volume of 1374.8 cm³, and the tube has a volume of 91.1 cm³ so that the
874 total system volume is 1465.934 cm³. The pumping rate is 0.351 per minute. The plastic chamber was equipped with an open
875 valve which was a necessity as the Dräger is an actively pumping system. Therefore, concentration increases in the chamber
876 can be considered as surface flow and as independent from pumping effects. The Measurement unit is protected by a preceding
877 2µm filter, preventing dust and vapor from entering the unit. Note that we use Flux values in this study only for relative
878 comparison and detection of the spatial variability of certain gas species and flows. A precise flux estimate is beyond the scope
879 of this publication and can not be constrained as we did not measure gas temperatures and humidity at sampling locations.

880 The measurement unit, a Dräger X-am 8000 handheld Multigas device was equipped with 6 sensors measuring CO₂, CH₄,
881 SO₂, H₂S, H₂, and O₂ simultaneously. The relevant species for this work are CO₂, SO₂, and H₂S, therefore only these will be
882 considered in detail. The CO₂ sensor is a Non-Dispersive Infrared (NDIR) sensor. NDIR sensors use the absorption
883 characteristics of CO₂ at ~ 4 µm, which leads to a concentration-dependent amplitude loss of the internally emitted IR light.
884 The sensor has a detection threshold of 0.01 vol% CO₂ and is calibrated for measuring CO₂ in a range of 0-5 vol% at a

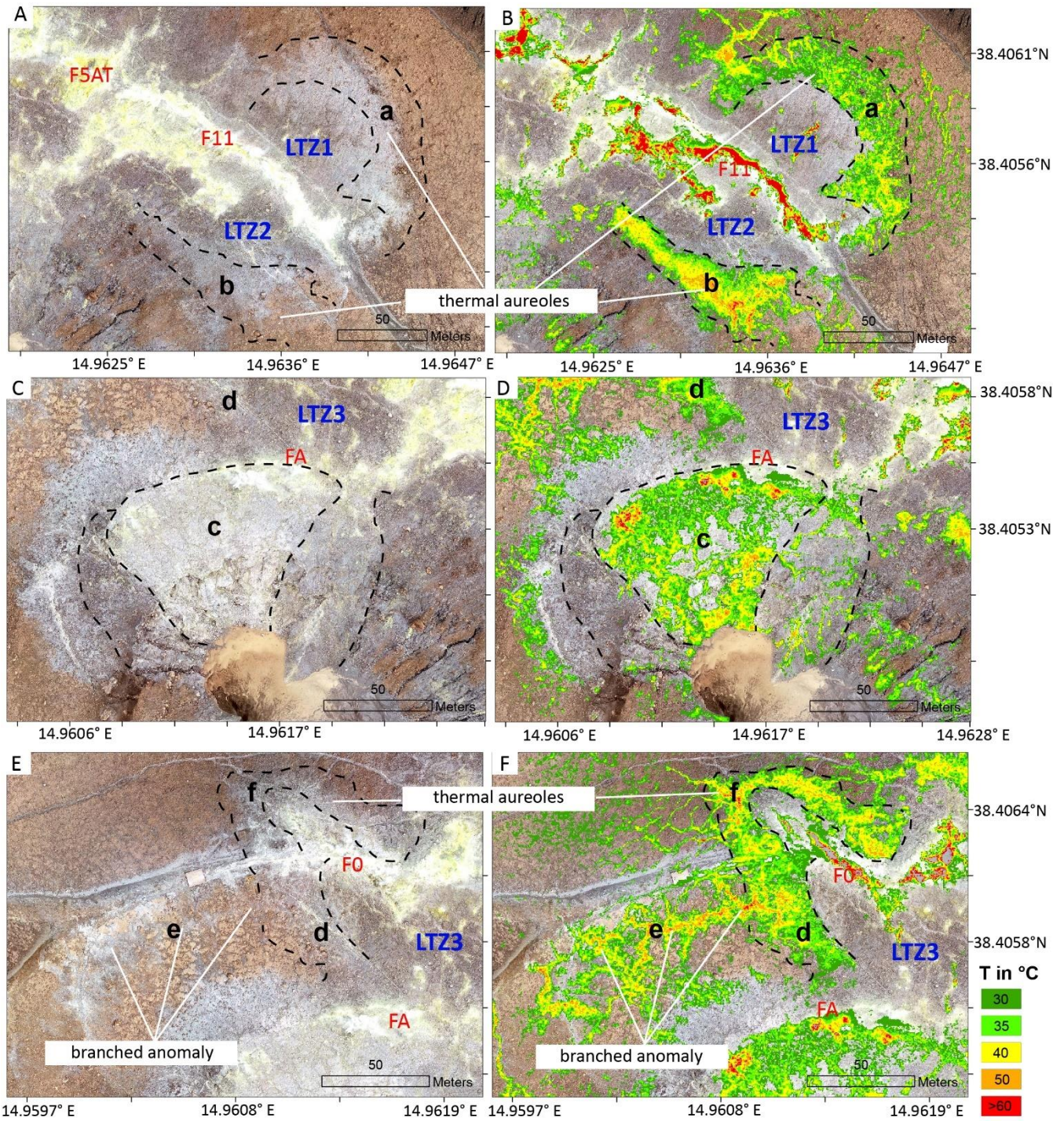
885 resolution of 50 ppm under normal (-20 - 50 °C, 10 - 95% RH, and 700 - 1300 hPa) atmospheric conditions. The response
886 rate is < 10 sec for reaching T50- and < 15 sec for reaching T90 concentrations. The H₂S sensor is an electrochemical sensor
887 with a detection limit of 0.4 ppm and a resolution of 0.1 ppm, measuring in a range of 0 - 100 ppm H₂S under normal
888 atmospheric conditions. The response time for T90 values is > 15 seconds and the accuracy of the measurement is +-5% of the
889 measured value. The SO₂ sensor is an electrochemical sensor with a detection limit of 0.1 ppm and a resolution of 0.1 ppm,
890 measuring as well in a range of 0-100 ppm under atmospheric conditions. The response time for T90 values is < 15 seconds
891 and the accuracy of the measurement is 2% of the measured value. The NDIR CO₂ sensor is robust against cross-sensitivities.
892 However, electrochemical sensors can be vulnerable to cross sensitivities (SO₂, H₂S, Cl₂), resulting in uncertainties of the
893 measurement of a few percent of the measurement value.

894 The approach of combining the Dräger Multigas with an accumulation chamber was developed and adapted as a consequence
895 of uncertainties encountered in previous campaigns. The different sensors have slightly different reaction times for ascending
896 gas concentrations and significantly different reaction times for descending gas concentrations. Comparing sensor readings
897 directly, therefore, might lead to odd gas ratios. For that reason, instead of the direct gas readings, we use the slope of the
898 ascending gas concentration within the accumulation chamber to produce more reliable estimates of the surface flow.

899 For a relative comparison of degassing rates of the single measurement points, the gas data was plotted and the representative
900 part of the graph, resembling a constantly ascending slope, was used to calculate the concentration increase by linear regression.
901 Data points of the “Dead Bands” at the beginning and end of each graph were removed. In this way, we achieve a relative gas
902 flux from surface that allows us to analyze spatial variations of gas flux throughout the study area. An overview of all gas
903 measurement points will be given in Figure 6. The aim of the gas measurements was not to provide accurate flux estimates but
904 to highlight and quantify the spatial variability of the surface flux of certain gas species.

905 Each measurement was performed under similar conditions. Locations were selected in a way that they represent similar
906 surface conditions, considering a spatial distance to fumarolic vents and an unsealed surface, for instance. Measurement
907 locations typically were small areas with a naturally “open surface”, often embedded in broader areas of the sealed surface.
908 Such spots typically can be identified by loose gravel on the surface and in case slightly different coloration. For the
909 measurement, the surface was cleaned and gravel was removed to provide a flat contact surface. Then the measurement was
910 started, and the plastic chamber was placed on the ground and sealed on the bottom with fine-grained material. The average
911 measurement duration was 2 min. In case of very rapidly ascending SO₂ or H₂S gas concentrations, the chamber was removed
912 from the ground before and the system was flooded with fresh air to protect the sensors from critically high acid concentrations.
913 This procedure was chosen to ensure a fresh air flooded chamber at the beginning of each measurement and to record the initial
914 background gas concentration. Further, it allows better identification of the measurement start- and end-points within the
915 respective data sets, as each data series has two dead bands, one at the beginning and one at the end. Figure B1 shows a typical
916 graph of a CO₂ measurement, with the Dead-Band at the beginning and end of each measurement and the constant ascending
917 graph, representing the gas concentration increase within the chamber. The “Dead Bands” represent parts of the measurement
918 where the accumulation chamber was placed on the ground but not sealed yet, or removed from the soil at the end of the
919 measurements. Dead Bands at the beginning of the measurement were typically on the order of 20 - 30 s.

920



923 Figure C1: Detail views of distinct units a - f and LTZ 1 - 3 in a true color representation as seen from our 2019 orthomosaic
924 data and an overlay by the thermal data with $T > 30\text{ }^{\circ}\text{C}$. A/B) Shown are units a and b and respective LTZ 1 and 2. Note the
925 outward spatial offset of both thermal units with respect to the surface coloration. C/D) Unit c is characterized by a network
926 of thermal anomalies embedded in the colder surroundings. E/F) Thermal aureole d and f, and branched anomaly e. Also here
927 an outward shift of the thermal feature with respect to the surface coloration is observed, which could indicate gradual sealing
928 processes with proximity to the main vents.

929
930

931 **Appendix D: Spearman correlation test for non-normal distributed variables**

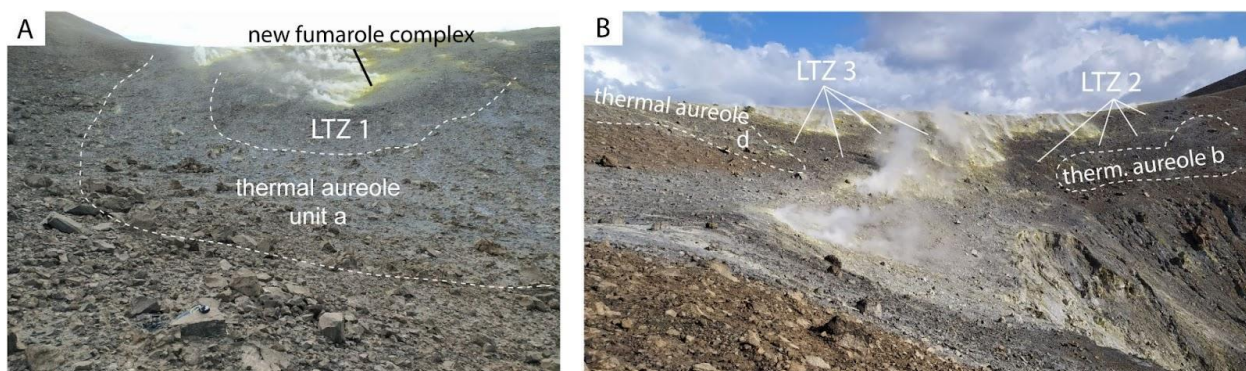
932 The test for correlation between optical and thermal anomalies was performed using the ggpubr package (Kassambara, 2019)
933 in the statistical software environment R. The method used was Spearman's rank correlation which is suggested to be used for
934 non-normal distributed data. The correlation test is based on the vectorized classification raster data set (classp_fumclip) with
935 8,890,830 data points with the analyzed variables pixel class (0 - 32) and pixel temperature (20 - 150 $^{\circ}\text{C}$). The results show a
936 correlation factor of 0.3485299, which is considered a mean positive correlation, and a p-value of $2.2\text{e-}16$ proves statistical
937 significance.

938

939 Spearman's rank correlation rho
940 data: x and y
941 $S = 7.6277\text{e+}19$, p-value $< 2.2\text{e-}16$
942 alternative hypothesis: true rho is not equal to 0
943 sample estimates:
944 rho
945 0.3485299

946
947

948 **Appendix E: Thermal aureoles and LTZ indicated in field photographs**



950 Figure E1: Thermal aureoles and Low-Temperature Zones (LTZ) depicted on field photographs. A) Thermal aureole a and
 951 LTZ 1. B) Thermal aureole b and d with LTZ 2 and LTZ 3.

952
 953
 954

955 **Appendix F: XRD results of samples taken along transects A and B**

956

957 Table F1: XRD results of samples taken along transects A and B

Sample ID	A1	A2	A3	A4	A5	A6	B1	B2	B3
Sanidine	86.7	85.7	87.4	61.5	72.2	60.3	68.2	49.2	0
Cristobalite	13.3	14.3	12.6	18.2	0	0	0	0	0
Coesite	0	0	0	0	0.7	0	0	0	0
Sulfur	0	0	0	20.3	25.1	39.7	31.8	50.8	100
Amorphous	50	0	0	0	0	50	50	0	0

958
 959
 960
 961

Appendix G: XRF results of samples taken along transects A-C.

962 Table G1: XRF results of samples taken along transects A-C. Note that samples with S > 10 % were not analyzed by XRF.

S-ID	SiO ₂ (%)	TiO ₂ (%)	Al ₂ O ₃ (%)	Fe ₂ O ₃ (%)	MnO (%)	MgO (%)	CaO (%)	Na ₂ O (%)	K ₂ O (%)	P ₂ O ₅ (%)	LOI (%)	S Eltra (%)
A1	76.0	0.2	10.7	1.6	0.1	0.1	1.1	1.8	4.8	0.1	3.8	0.1
A2	76.2	0.4	10.6	1.5	0.1	0	0.8	1.5	5.0	0.1	3.9	0.3
A3	77.0	0.3	10.2	1.4	0.1	0	0.7	1.6	4.8	0.1	4.3	0.2
A4	x	x	x	x	x	x	x	x	x	x	x	11.7
A5	67.3	2.2	0.4	0.3	11.9	0.1	1.2	3.1	5.0	0.1	2.0	6.0
A6	71.0	1.2	0.3	0.3	6.7	0.0	0.4	1.3	2.7	0.0	9.8	6.3
B1	73.0	1.2	0.3	0.3	7.0	0.0	0.5	1.3	3.0	0.0	4.3	9.0

B2	x	x	x	x	x	x	x	x	x	x	x	31.9
B3	x	x	x	x	x	x	x	x	x	x	x	60.5
C1	69.7	0.4	8.4	2.0	0	0.3	1.0	2.4	4.2	0.1	11.3	0.1
C2	81.3	0.3	6.1	1.1	0	0.1	0.4	1.1	2.5	0	6.1	0.5
C3	77.4	0.4	7.6	1.8	0	0.2	0.9	2.0	4.0	0.1	5.1	0.4
C4	x	x	x	x	x	x	x	x	x	x	x	40.3
C5	x	x	x	x	x	x	x	x	x	x	x	26.2
C6	x	x	x	x	x	x	x	x	x	x	x	12.5
C7	x	x	x	x	x	x	x	x	x	x	x	17.5
C8	63.8	0.4	12.0	3.2	0.1	0.4	1.7	5.0	8.0	0.1	3.2	1.2
C9	68.9	0.4	11.4	1.5	0	0.4	1.3	3.0	4.7	0.1	8.1	0.2

963
964
965

10 Data availability

966 The remote sensing data used for this study and relevant processing steps are published in a Zenodo data repository
967 <https://doi.org/10.5281/zenodo.12586672>. Other data will be made available on request.

968 11 Author contributions

969 D.M conceptualized the study, collected data, performed the remote sensing and gas analysis, and led the manuscript writing.
970 T.R.W. provided funding, supported the conceptualization, and supervised the writing. V.T. supported the conceptualization,
971 performed XRD analysis, and supervised the writing. J.S. performed XRF analysis and supported the writing. A.K. performed
972 XRD analysis and supported the writing. E.D.P. collected data and samples, supported all field works and the writing of this
973 manuscript. A.F.P. supported fieldwork and on the ground logistics, acquired data, and supported the writing. M.Z. supported
974 the gas measurement campaign and supported the writing. B.D.J. supported the fieldwork and writing of this manuscript.
975

976 12 Competing interests

977 The authors declare that they have no conflict of interest.

978 **13 Acknowledgements**

979 We are grateful for the financial and material support provided to realize this study. This work is contributing to the focus site
980 Etna and was financially supported by GFZ Potsdam. Financial support to realize this study was also provided by DAAD
981 research grant Nr. 57556282 and by ERC project ‘ROTTnROCK*, a research project funded by the European Research
982 Council under the European Union’s Horizon Europe Programme / ERC synergy grant n. [ERC-2023-SyG 101118491]. We
983 furthermore thank INGV Palermo for collaboration and support, especially during the 2021 crisis, without which parts of this
984 study could not have been realized.

985 **14 References**

986 Abdi, H., and Williams, L. J.: Principal component analysis, Wiley Interdiscip. Rev. Comput. Stat., 2(4), 433-459,
987 <https://doi.org/10.1002/wics.101>, 2010.

988
989 Aiuppa, A., Federico, C., Giudice, G., and Gurrieri, S.: Chemical mapping of a fumarolic field: La Fossa crater, Vulcano Island
990 (Aeolian Islands, Italy), GEOPHYS RES LETT, 32(13), <https://doi.org/10.1029/2005GL023207>, 2005.

991
992 Alexandris, N., Gupta, S., and Koutsias, N.: Remote sensing of burned areas via PCA, Part 1; centering, scaling and EVD vs
993 SVD, Open geospat. data, softw. stand., 2, 1-11, <https://doi.org/10.1186/s40965-017-0028-1>, 2017.

994
995 Azzarini, F. M., Pareschi, M. T., Sbrana, A., Favalli, M., and Fulignati, P.: Surface hydrothermal alteration mapping at Vulcano
996 Island using MIVIS data, Int. J. Remote Sens., 22(11), 2045-207, <https://doi.org/10.1080/01431160118291>, 2001.

997
998 Ball, M. and Pinkerton, H.: Factors affecting the accuracy of thermal imaging cameras in volcanology, J GEOPHYS RES-
999 SOL EA, 111(B11), <https://doi.org/10.1029/2005JB003829>, 2006.

1000
1001 Barreca, G., Bruno, V., Cultrera, F., Mattia, M., Monaco, C., and Scarfi, L.: New insights in the geodynamics of the Lipari-
1002 Vulcano area (Aeolian Archipelago, southern Italy) from geological, geodetic and seismological data, J. Geodyn., 82, 150-
1003 167, <https://doi.org/10.1016/j.jog.2014.07.003>, 2014.

1004
1005 Berg, S. E., Troll, V. R., Harris, C., Deegan, F. M., Riishuus, M. S., Burchardt, S., and Krumbholz, M.: Exceptionally high
1006 whole-rock $\delta^{18}\text{O}$ values in intra-caldera rhyolites from Northeast Iceland, Mineral. Mag., 82(5), 1147-1168,
1007 <https://doi.org/10.1180/mgm.2018.114>, 2018.

1008
1009 Billi, A., Barberi, G., Faccenna, C., Neri, G., Pepe, F., and Sulli, A.: Tectonics and seismicity of the Tindari Fault System,
1010 southern Italy: Crustal deformations at the transition between ongoing contractional and extensional domains located above
1011 the edge of a subducting slab, TECTONICS, 25(2), <https://doi.org/10.1029/2004TC001763>, 2006.

1012
1013 Bolognesi, L., and D'Amore, F.: Isotopic variation of the hydrothermal system on Vulcano Island, Italy. GEOCHIM
1014 COSMOCHIM AC, 57(9), 2069-2082, [https://doi.org/10.1016/0016-7037\(93\)90094-D](https://doi.org/10.1016/0016-7037(93)90094-D), 1993.

1015

1016 Boyce, A. J., Fulignati, P., Sbrana, A., and Fallick, A. E.: Fluids in early stage hydrothermal alteration of high-sulfidation
1017 epithermal systems: A view from the Vulcano active hydrothermal system (Aeolian Island, Italy), *J VOLCANOL GEOTH*
1018 *RES*, 166(2), 76-90, <https://doi.org/10.1016/j.jvolgeores.2007.07.005>, 2007.
1019

1020 Bukumirovic, T., Italiano, F., and Nuccio, P. M.: The evolution of a dynamic geological system: the support of a GIS for
1021 geochemical measurements at the fumarole field of Vulcano, Italy, *J VOLCANOL GEOTH RES*, 79(3-4), 253-263,
1022 [https://doi.org/10.1016/S0377-0273\(97\)00032-2](https://doi.org/10.1016/S0377-0273(97)00032-2), 1997.
1023

1024 Capasso, G., Favara, R., and Inguaggiato, S.: Chemical features and isotopic composition of gaseous manifestations on
1025 Vulcano Island, Aeolian Islands, Italy: an interpretative model of fluid circulation. *GEOCHIM COSMOCHIM AC*, 61, 3425–
1026 3440, [https://doi.org/10.1016/S0016-7037\(97\)00163-4](https://doi.org/10.1016/S0016-7037(97)00163-4), 1997.
1027

1028 Capasso, G., Favara, R., and Inguaggiato, S.: Interaction between fumarolic gases and thermal groundwaters at Vulcano Island
1029 (Italy): evidences from chemical composition of dissolved gases in waters, *J VOLCANOL GEOTH RES*, 102(3-4), 309-
1030 318, [https://doi.org/10.1016/S0377-0273\(00\)00193-1](https://doi.org/10.1016/S0377-0273(00)00193-1), 2000.
1031

1032 Capasso, G., Federico, C., Madonia, P., and Paonita, A.: Response of the shallow aquifer of the volcano-hydrothermal system
1033 during the recent crises at Vulcano Island (Aeolian Archipelago, Italy), *J VOLCANOL GEOTH RES*, 273, 70-80,
1034 <https://doi.org/10.1016/j.jvolgeores.2014.01.005>, 2014.
1035

1036 Carapezza, M. L., Barberi, F., Ranaldi, M., Ricci, T., Tarchini, L., Barrancos, J., Fischer, C., Perez, N., Weber, K., Di Piazza,
1037 A., and Gattuso, A.: Diffuse CO₂ soil degassing and CO₂ and H₂S concentrations in air and related hazards at Vulcano Island
1038 (Aeolian arc, Italy). *J VOLCANOL GEOTH RES*, 207(3-4), 130-144, <https://doi.org/10.1016/j.jvolgeores.2011.06.010>, 2011.
1039

1040 Carranza, E. J. M., and Hale, M.: Mineral imaging with Landsat Thematic Mapper data for hydrothermal alteration mapping
1041 in heavily vegetated terrane, *Int. J. Remote Sens*, 23(22), 4827-4852, <https://doi.org/10.1080/01431160110115014>, 2002.
1042

1043 Chiodini, G., Cioni, R., and Marini, L.: Reactions governing the chemistry of crater fumaroles from Vulcano Island, Italy, and
1044 implications for volcanic surveillance, *APPL GEOCHEM*, 8(4), 357-371, [https://doi.org/10.1016/0883-2927\(93\)90004-Z](https://doi.org/10.1016/0883-2927(93)90004-Z),
1045 1993.
1046

1047 Chiodini G., Cioni R., Marini L. and Panichi C.: Origin of fumarolic fluids of Vulcano Island, Italy and implications for
1048 volcanic surveillance, *B VOLCANOL*, 57, 99–110, <http://dx.doi.org/10.1007/BF00301400>, 1995.
1049

1050 Chiodini, G., Allard, P., Caliro, S., and Parello, F.: 18O exchange between steam and carbon dioxide in volcanic and
1051 hydrothermal gases: Implications for the source of water, *GEOCHIM COSMOCHIM AC* , 64, 2479–2488,
1052 [https://doi.org/10.1016/S0016-7037\(99\)00445-7](https://doi.org/10.1016/S0016-7037(99)00445-7), 2000.
1053

1054 Chiodini, G., Frondini, F., and Raco, B.: Diffuse emission of CO₂ from the Fossa crater, Vulcano Island (Italy), *B*
1055 *VOLCANOL*, 58, 41-50, <https://doi.org/10.1007/s004450050124>, 1996.
1056

1057 Chiodini, G., Granieri, D., Avino, R., Caliro, S., Costa, A., and Werner, C.: Carbon dioxide diffuse degassing and estimation
1058 of heat release from volcanic and hydrothermal systems, *J GEOPHYS RES-SOL EA*, 110(B8),
1059 <https://doi.org/10.1029/2004JB003542>, 2005.
1060

1061 Clarke, A. B., Ongaro, T. E., and Belousov, A.: Vulcanian eruptions. In *The encyclopedia of volcanoes*, Academic Press, pp.
1062 505-518, <https://doi.org/10.1016/B978-0-12-385938-9.00028-6>, 2015.
1063

1064 Coppola, D., Laiolo, M., Campus, A., and Massimetti, F.: Thermal unrest of a fumarolic field tracked using VIIRS imaging
1065 bands: The case of La Fossa crater (Vulcano Island, Italy), *FRONT EARTH SCI*, 10, 964372,
1066 <https://doi.org/10.3389/feart.2022.964372>, 2022.
1067

1068 Cultrera F., Barreca G., Ferranti L., Monaco C., Pepe F., Passaro S., Barberi G., Bruno V., Burrato P., Mattia M., Musumeci
1069 C., Scarfì L.: Structural architecture and active deformation pattern in the northern sector of the Aeolian-Tindari-Letojanni
1070 fault system (SE Tyrrhenian Sea-NE Sicily) from integrated analysis of field, marine geophysical, seismological and geodetic
1071 data, *ITAL J GEOSCI*, 136 (3), 399–417, <https://doi.org/10.3301/IJG.2016.17>, 2017.
1072

1073 Darmawan, H., Troll, V. R., Walter, T. R., Deegan, F. M., Geiger, H., Heap, M. J., Searphine, N., Harris, C., Humaida, H.,
1074 and Müller, D.: Hidden mechanical weaknesses within lava domes provided by buried high-porosity hydrothermal alteration
1075 zones, *SCI REP-UK*, 12(1), 3202, <https://doi.org/10.1038/s41598-022-06765-9>, 2022.
1076

1077 De Astis, G., La Volpe, L., Peccerillo, A., and Civetta, L.: Volcanological and petrological evolution of Vulcano island
1078 (Aeolian Arc, southern Tyrrhenian Sea), *J GEOPHYS RES-SOL EA*, 102(B4), 8021-8050,
1079 <https://doi.org/10.1029/96JB03735>, 1997.
1080

1081 De Astis, G., Lucchi, F., Dellino, P., La Volpe, L., Tranne, C. A., Frezzotti, M. L., and Peccerillo, A.: Chapter 11 Geology,
1082 volcanic history and petrology of Vulcano (central Aeolian archipelago), *Geol Soc Lond Mem*, 37(1), 281-349,
1083 <https://doi.org/10.1144/M37.11>, 2013.
1084

1085 Di Tommaso, I., and Rubinstein, N.: Hydrothermal alteration mapping using ASTER data in the Infiernillo porphyry deposit,
1086 Argentina, *ORE GEOL REV*, 32(1-2), 275-290, <https://doi.org/10.1016/j.oregeorev.2006.05.004>, 2007.
1087

1088 Diliberto, I. S.: Time series analysis of high temperature fumaroles monitored on the island of Vulcano (Aeolian Archipelago,
1089 Italy), *J VOLCANOL GEOTH RES*, 264, 150-163, <https://doi.org/10.1016/j.jvolgeores.2013.08.003>, 2013.
1090

1091 Diliberto, I. S.: Long-term monitoring on a closed-conduit volcano: A 25 year long time-series of temperatures recorded at La
1092 Fossa cone (Vulcano Island, Italy), ranging from 250 C to 520 C, *J VOLCANOL GEOTH RES*, 346, 151-160,
1093 <https://doi.org/10.1016/j.jvolgeores.2017.03.005>, 2017.
1094

1095 Diliberto, I., Pedone, M., Jácome Paz, M., Inguaggiato, S., Mazot, A., Cangemi, M. and Pisciotta, A.F.: Volcanic Gas Hazard
1096 Assessment in the Baia di Levante Area (Vulcano Island, Italy) Inferred by Geochemical Investigation of Passive Fluid
1097 Degassing. *Environ Geosci*, 11(11), 478, <https://doi.org/10.3390/geosciences11110478>, 2021.
1098

1099 Donoghue, E., Troll, V. R., Harris, C., O'Halloran, A., Walter, T. R., and Torrado, F. J. P.: Low-temperature hydrothermal
1100 alteration of intra-caldera tuffs, Miocene Tejeda caldera, Gran Canaria, Canary Islands, *J VOLCANOL GEOTH RES*, 176(4),
1101 551-564, <https://doi.org/10.1016/j.jvolgeores.2008.05.002>, 2008.
1102
1103 Donoghue, E., Troll, V. R., and Harris, C.: Fluid–rock interaction in the Miocene, Post-Caldera, Tejeda intrusive complex,
1104 Gran Canaria (Canary Islands): insights from mineralogy, and O-and H-isotope geochemistry, *J PETROL*, 51(10), 2149-2176,
1105 <https://doi.org/10.1093/petrology/egq052>, 2010.
1106
1107 Fauvel, M., Chanussot, J., and Benediktsson, J. A.: Kernel principal component analysis for the classification of hyperspectral
1108 remote sensing data over urban areas, *EURASIP JASP*, 1-14, <https://doi.org/10.1155/2009/783194>, 2009.
1109
1110 Fischer, T. P., Ramírez, C., Mora-Amador, R. A., Hilton, D. R., Barnes, J. D., Sharp, Z. D., Le Brun, M., de Moor, J.M., Barry,
1111 P.H., Füre, E., and Shaw, A. M.: Temporal variations in fumarole gas chemistry at Poás volcano, Costa Rica. *J VOLCANOL*
1112 *GEOTH RES*, 294, 56-70, <https://doi.org/10.1016/j.jvolgeores.2015.02.002>, 2015.
1113
1114 Frolova, et al. Effects of hydrothermal alterations on physical and mechanical properties of rocks in the Kuril–Kamchatka
1115 island arc, *ENG GEOL*, 183, 80-95, <https://doi.org/10.1016/j.enggeo.2014.10.011>, 2014.
1116
1117 Fulignati, P., Gioncada, A., and Sbrana, A.: Geologic model of the magmatic-hydrothermal system of vulcano (Aeolian
1118 Islands, Italy), *MINER PETROL*, 62(3-4), 195, 1998.
1119
1120 Fulignati, P., Gioncada, A., and Sbrana, A.: Rare-earth element (REE) behaviour in the alteration facies of the active
1121 magmatic–hydrothermal system of Vulcano (Aeolian Islands, Italy), *J VOLCANOL GEOTH RES*, 88(4), 325-342,
1122 [https://doi.org/10.1016/S0377-0273\(98\)00117-6](https://doi.org/10.1016/S0377-0273(98)00117-6), 1999.
1123
1124 Fulignati, P.: Clay minerals in hydrothermal systems, *Minerals*, 10(10), 919, <https://doi.org/10.3390/min10100919>, 2020.
1125
1126 Gertisser, R., Troll, V. R., Walter, T. R., Nandaka, I. G. M. A., and Ratdomopurbo, A.: Merapi Volcano: Geology, Eruptive
1127 Activity, and Monitoring of a High-Risk Volcano, Springer *NATURE*, <https://doi.org/10.1007/978-3-031-15040-1>, 2023.
1128
1129 Giggenbach, W.F.: Chemical Composition of Volcanic Gases. In: *Monitoring and Mitigation of Volcano Hazards*. Springer,
1130 Berlin, Heidelberg, https://doi.org/10.1007/978-3-642-80087-0_7, 1996.
1131
1132 Halldórsson, S. A., Hilton, D. R., Troll, V. R., and Fischer, T. P.: Resolving volatile sources along the western Sunda arc,
1133 Indonesia, *CHEM GEOL*, 339, 263-282, <https://doi.org/10.1016/j.chemgeo.2012.09.042>, 2013.
1134
1135 Harris, A. J., Lodato, L., Dehn, J., and Spampinato, L.: Thermal characterization of the Vulcano fumarole field, *B*
1136 *VOLCANOL*, 71, 441-458, <https://doi.org/10.1007/s00445-008-0236-8>, 2009.
1137
1138 Harris, A., Alparone, S., Bonforte, A., Dehn, J., Gambino, S., Lodato, L., and Spampinato, L.: Vent temperature trends at the
1139 Vulcano Fossa fumarole field: the role of permeability, *B VOLCANOL*, 74, 1293-1311, [https://doi.org/10.1007/s00445-012-](https://doi.org/10.1007/s00445-012-0593-1)
1140 [0593-1](https://doi.org/10.1007/s00445-012-0593-1), 2012.

1141
1142 Heap, M.J., Troll, V.R., Kushnir, A.R.L., Gilg, H.A., Collinson, A.S.D., Deegan, F.M., Darmawan, H., Seraphine, N., Neuberg,
1143 J. and Walter, T.R.: Hydrothermal alteration of andesitic lava domes can lead to explosive volcanic behaviour, *Nat Commun*,
1144 10(1), 5063, <https://doi.org/10.1038/s41467-019-13102-8>, 2019.
1145
1146 Heap, M. J., and Violay, M. E.: The mechanical behaviour and failure modes of volcanic rocks: a review, *B VOLCANOL*,
1147 83(5), 33, <https://doi.org/10.1007/s00445-021-01447-2>, 2021.
1148
1149 Heap, M. J., Baumann, T. S., Rosas-Carbajal, M., Komorowski, J. C., Gilg, H. A., Villeneuve, M., Moretti, R., Baud, P.,
1150 Carbillet, L., Harnett, C., and Reuschlé, T.: Alteration-Induced Volcano Instability at La Soufrière de Guadeloupe (Eastern
1151 Caribbean), *J GEOPHYS RES-SOL EA*, 126(8), e2021JB022514, <https://doi.org/10.1029/2021JB022514>, 2021.
1152
1153 Heap, M. J., Baumann, T., Gilg, H. A., Kolzenburg, S., Ryan, A. G., Villeneuve, M., Russel, J.K., Kennedy, L.A., Rosas-
1154 Carbajal, M., and Clynne, M. A.: Hydrothermal alteration can result in pore pressurization and volcano instability. *GEOLOGY*,
1155 49(11), 1348-1352, <https://doi.org/10.1130/G49063.1>, 2021.
1156
1157 Henley, R. W., and McNabb, A.: Magmatic vapor plumes and ground-water interaction in porphyry copper emplacement,
1158 *ECON GEOL*, 73(1), 1-20, <https://doi.org/10.2113/gsecongeo.73.1.1>, 1978.
1159
1160 Inguaggiato, S., Vita, F., Diliberto, I. S., Inguaggiato, C., Mazot, A., Cangemi, M., and Corrao, M.: The volcanic activity
1161 changes occurred in the 2021–2022 at Vulcano island (Italy), inferred by the abrupt variations of soil CO₂ output, *SCI REP-*
1162 *UK*, 12(1), 21166, <https://doi.org/10.3390/rs14051283>, 2022.
1163
1164 Kassambara, A.: ggpubr: 'ggplot2' based publication ready plots. R package version 0.4. 0., 2020.
1165
1166 Kereszturi, G., Schaefer, L. N., Miller, C., and Mead, S.: Hydrothermal alteration on composite volcanoes: mineralogy,
1167 hyperspectral imaging, and aeromagnetic study of Mt Ruapehu, New Zealand, *GEOCHEM GEOPHY GEOSY*, 21(9),
1168 e2020GC009270, <https://doi.org/10.1029/2020GC009270>, 2020.
1169
1170 Liuzzo, M., Di Muro, A., Giudice, G., Michon, L., Ferrazzini, V., and Gurrieri, S.: New evidence of CO₂ soil degassing
1171 anomalies on Piton de la Fournaise volcano and the link with volcano tectonic structures, *GEOCHEM GEOPHY GEOSY*,
1172 16(12), 4388-4404, <https://doi.org/10.1002/2015GC006032>, 2015.
1173
1174 Loughlin, W. P.: Principal component analysis for alteration mapping, *PHOTOGRAMM ENG REM S*, 57(9), 1163-1169,
1175 1991.
1176
1177 Lynch, D.K., Hudnut, K.W. and Adams, P.M.: Development and growth of recently-exposed fumarole fields near Mullet
1178 Island, Imperial County, California, *GEOMORPHOLOGY*, 195, 27-44, <https://doi.org/10.1016/j.geomorph.2013.04.022>,
1179 2013.
1180
1181 Madonia, P., Cusano, P., Diliberto, I. S., and Cangemi, M.: Thermal anomalies in fumaroles at Vulcano island (Italy) and their
1182 relationship with seismic activity, *PHYS CHEM EARTH PT ABC*, 63, 160-169, <https://doi.org/10.1016/j.pce.2013.06.001>,
1183 2013.

1184

1185 Madonia, P., Cangemi, M., Costa, M., and Madonia, I.: Mapping fumarolic fields in volcanic areas: A methodological approach
1186 based on the case study of La Fossa cone, Vulcano island (Italy), *J VOLCANOL GEOTH RES*, 324, 1-
1187 7, <https://doi.org/10.1016/j.jvolgeores.2016.05.014>, 2016.

1188

1189 Mannini, S., Harris, A. J., Jessop, D. E., Chevrel, M. O., and Ramsey, M. S.: Combining ground-and ASTER-based thermal
1190 Measurements to Constrain fumarole field heat budgets: The case of Vulcano Fossa 2000–2019, *Geophys. Res. Lett.*, 46(21),
1191 11868-11877, <https://doi.org/10.1029/2019GL084013>, 2019.

1192

1193 Mia, B., and Fujimitsu, Y.: Mapping hydrothermal altered mineral deposits using Landsat 7 ETM+ image in and around Kuju
1194 volcano, Kyushu, Japan. *J EARTH SYST SCI*, 121, 1049-1057, <https://doi.org/10.1007/s12040-012-0211-9>, 2012.

1195

1196 Middlemost, E. A.: Naming materials in the magma/igneous rock system. *Earth-Sci Rev*, 37(3-4), 215-224,
1197 [https://doi.org/10.1016/0012-8252\(94\)90029-9](https://doi.org/10.1016/0012-8252(94)90029-9), 1994.

1198

1199 Minissale, A., Donato, A., Procesi, M., Pizzino, L. and Giammanco, S.: Systematic review of geochemical data from thermal
1200 springs, gas vents and fumaroles of Southern Italy for geothermal favourability mapping, *Earth-Sci Rev*, 188, 514-535,
1201 <https://doi.org/10.1016/j.earscirev.2018.09.008>, 2019.

1202

1203 Müller, D., Bredemeyer, S., Zorn, E., De Paolo, E., and Walter, T. R.: Surveying fumarole sites and hydrothermal alteration
1204 by unoccupied aircraft systems (UAS) at the La Fossa cone, Vulcano Island (Italy), *J VOLCANOL GEOTH RES*, 413, 107208,
1205 <https://doi.org/10.1016/j.jvolgeores.2021.107208>, 2021.

1206

1207 Müller, D., Walter, T. R., Troll, V. R., Stammeier, J., Karlsson, A., De Paolo, E., Pisciotta, F. A., Zimmer, M., and DeJarnatt,
1208 B.: Data set: UAS-based optical- and thermal infrared remote sensing of the fumarole field of La Fossa cone, Vulcano Island
1209 (Italy), reveals the degassing and hydrothermal alteration structure, Zenodo. <https://doi.org/10.5281/zenodo.12586672>, 2024.

1210

1211 Nuccio, P. M., and Paonita, A.: Magmatic degassing of multicomponent vapors and assessment of magma depth: application
1212 to Vulcano Island (Italy), *EARTH PLANET SC LETT*, 193(3-4), 467-481, [https://doi.org/10.1016/S0012-821X\(01\)00512-X](https://doi.org/10.1016/S0012-821X(01)00512-X),
1213 2001.

1214

1215 Paonita, A., Federico, C., Bonfanti, P., Capasso, G., Inguaggiato, S., Italiano, F., Madonia, P., Pecoraino, G., and Sortino, F.:
1216 The episodic and abrupt geochemical changes at La Fossa fumaroles (Vulcano Island, Italy) and related constraints on the
1217 dynamics, structure, and compositions of the magmatic system, *GEOCHIM COSMOCHIM AC*, 120, 158-
1218 178, <https://doi.org/10.1016/j.gca.2013.06.015>, 2013.

1219

1220 Pearson, K. F.R.S.: On lines and planes of closest fit to systems of points in space, *Lond.Edinb.Dubl.Phil.Mag.*, 2(11), 559–
1221 572, <https://doi.org/10.1080/14786440109462720>, 1901.

1222

1223 Pirajno, F.: Hydrothermal Processes and Wall Rock Alteration. In: *Hydrothermal Processes and Mineral Systems*, Springer,
1224 Dordrecht, https://doi.org/10.1007/978-1-4020-8613-7_2, 2009.

1225

1226 Reid, M. E., Sisson, T. W., and Brien, D. L.: Volcano collapse promoted by hydrothermal alteration and edifice shape, Mount
1227 Rainier, Washington, GEOLOGY, 29(9), 779-782, [https://doi.org/10.1130/0091-7613\(2001\)029%3C0779:VCPBHA%3E2.0.CO;2](https://doi.org/10.1130/0091-7613(2001)029%3C0779:VCPBHA%3E2.0.CO;2), 2001.

1229

1230 Rowan, L. C., Wetlaufer, P. H., and Stewart, J. H.: Discrimination of rock Types and detection of hydrothermally altered areas
1231 in south-central Nevada by the use of computer-enhanced ERTS images, 1976.

1232

1233 Silvestri, M., Rabuffi, F., Pisciotta, A., Musacchio, M., Diliberto, I. S., Spinetti, C., Lombardo, V., Colini, L., and Buongiorno,
1234 M. F.: Analysis of thermal anomalies in volcanic areas using multiscale and multitemporal monitoring: Vulcano island test
1235 case, Remote Sens., 11(2), 134, <https://doi.org/10.3390/rs11020134>, 2019.

1236

1237 Stevenson, J.A. and Varley, N.: Fumarole monitoring with a handheld infrared camera: Volcán de Colima, Mexico, 2006–
1238 2007, J VOLCANOL GEOTH RES, 177(4), pp.911-924, <https://doi.org/10.1016/j.jvolgeores.2008.07.003>, 2008.

1239

1240 Tayebi, M.H., Tangestani, M.H. and Vincent, R.K.: Sub-pixel mapping of iron-bearing minerals using ALI data and MTMF
1241 algorithm, Masahim volcano, SE Iran., Arab J Geosci 8, 3799–3810, <https://doi.org/10.1007/s12517-014-1400-4>, 2015.

1242

1243 Troll, V. R., Hilton, D. R., Jolis, E. M., Chadwick, J. P., Blythe, L. S., Deegan, F. M., Schwartzkopf, L.M., and Zimmer, M.:
1244 Crustal CO₂ liberation during the 2006 eruption and earthquake events at Merapi volcano, Indonesia, Geophys. Res. Lett.,
1245 39(11), <https://doi.org/10.1029/2012GL051307>, 2012.

1246

1247 Toutain, J.-P., Sortino, F., Baubron, J.-C., Richon, P., Surono, Sumarti, S. and Nonell, A.: Structure and CO₂ budget of Merapi
1248 volcano during inter-eruptive periods, B Volcanol, 71(7), 815-826, <https://doi.org/10.1007/s00445-009-0266-x>, 2009.

1249

1250 Van der Meer, F. D., Van der Werff, H. M., Van Ruitenbeek, F. J., Hecker, C. A., Bakker, W. H., Noomen, M. F., Van der
1251 Meijde, M., Carranza, E.J.M., Boudewijn de Smeth, J., and Woldai, T.: Multi-and hyperspectral geologic remote sensing: A
1252 review, INT J APPL EARTH OBS, 14(1), 112-128, <https://doi.org/10.1016/j.jag.2011.08.002>, 2012.

1253

1254

1255